

# Lithospheric deformation during the early stages of continental collision: Numerical experiments and comparison with South Island, New Zealand

Russell N. Pysklywec

Department of Geology, University of Toronto, Ontario, Canada

Christopher Beaumont and Philippe Fullsack

Department of Oceanography, Dalhousie University, Halifax, Nova Scotia, Canada

Received 26 January 2001; revised 18 November 2001; accepted 23 November 2001; published 16 July 2002.

[1] The nature of lithospheric deformation during continental plate collision still remains unresolved. While it has often been proposed that the mantle lithosphere is accommodated by distributed thickening of a viscous root, an alternate hypothesis suggests that significant portions of convergent mantle lithosphere essentially undergo underthrusting or subduction. To further consider this issue, we model the thermochemical evolution of the lithosphere-mantle system using arbitrary Lagrangian-Eulerian finite element techniques. We incorporate a mix of viscous (thermally activated power law creep) and plastic (frictional Coulomb with strain softening) rheologies in the numerical experiments to treat disparate composition in the crust and mantle. A range of rheological and mechanical parameters is explored to determine controls on the style of lithospheric deformation. The models suggest that during the initial stages of plate collision the mantle lithosphere is characterized by plate-like behavior and underthrusting/subduction of the upper region in conjunction with distributed thickening and Rayleigh-Taylor type viscous instability of the lower portion. Depending on the material rheology, temperature regime, and imposed convergence velocity, the deforming mantle lithosphere demonstrates various combinations of these “end-member” behavioral modes. The modeling results are interpreted in the context of observed lithospheric deformation across South Island, New Zealand. A combined style of underthrusting and distributed thickening is consistent with the observed crustal structure in the young collisional orogen as well as seismic imaging of the geometry of the underlying lithosphere.

**INDEX TERMS:** 8102 Tectonophysics: Continental contractional orogenic belts; 8120 Tectonophysics: Dynamics of lithosphere and mantle—general; 8150 Evolution of the Earth: Plate boundary—general (3040); 8158 Evolution of the Earth: Plate motions—present and recent (3040); **KEYWORDS:** New Zealand, orogenesis, mantle lithosphere, numerical modeling, subduction, continental collision

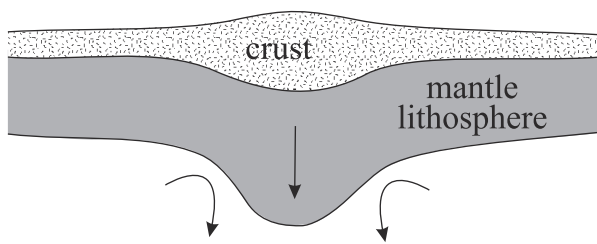
## 1. Introduction

[2] With the development of the theory of plate tectonics, a framework was established to understand the motion of mobile tectonic plates and the dynamic evolution of the lithosphere at the plate boundaries [e.g., *Wilson, 1965*]. At convergent ocean-continent or ocean-ocean plate boundaries, for example, geological and geophysical observation suggests that collision is accommodated by coherent subduction of one plate beneath the other along a discrete shear zone. While there is still much to be learned about details of the process (e.g., initiation of subduction, fate of the slabs at depth), subduction is fundamental to all episodes of oceanic plate convergence.

[3] The dynamics of continent-continent plate boundaries are less well known. Crustal convergence is usually accom-

modated by significant thickening, heating, and internal deformation, which result in the development of a collisional mountain belt parallel to the plate boundary. Aspects of crustal evolution during such orogenesis may be deduced through direct observation of surface geology, indirect methods of geophysical (e.g., seismic, electromagnetic, gravity) imaging at depth, and interpretation with geodynamical modeling. More difficult to determine is the behavior of the lower portions of the lithosphere, that is, the dynamics at the crust-mantle interface, and the evolution of the subcrustal lithosphere (the mantle lithosphere). While future initiatives may better resolve the lower lithosphere [e.g., *Levander et al., 1999*], conventional geophysical probing of the region has been hindered by the depth in the Earth and the thick sequences of often highly deformed material in the overlying crustal orogen. As a result, even the first-order behavior of the mantle lithosphere during continental plate convergence is uncertain and remains a gap in the understanding of plate tectonics.

## (a) gravitational (RT) instability



## (b) subduction/underthrusting

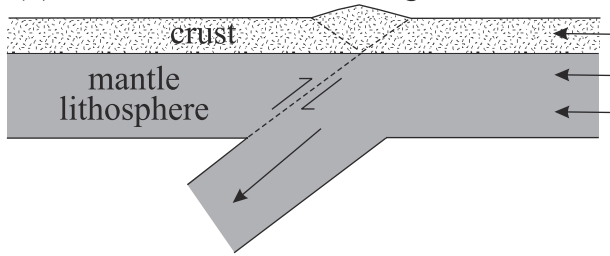


**Figure 1.** Conceptual illustrations of two potential mechanisms of mantle lithosphere deformation during orogenesis: (a) gravitational Rayleigh-Taylor instability of viscous mantle lithosphere; (b) subduction/underthrusting of convergent mantle lithosphere along a mantle shear zone.

[4] *Houseman et al.* [1981] first proposed that during continental plate convergence, the mantle lithosphere is accommodated by distributed lithospheric thickening followed by convective removal of a viscous subcrustal root. They argued that the lower part of a dense thickened lithosphere (e.g., in a convergent zone) is gravitationally unstable and under certain conditions may develop as a Rayleigh-Taylor-type mantle downwelling. In the case of the Tibetan Plateau, as an example, this mechanism has been invoked to account for the inferred large-scale uplift of the region since the Miocene [*England and Houseman*, 1989]. Subsequent studies have demonstrated that rheological variations such as temperature dependence [e.g., *Buck and Toksöz*, 1983; *Lenardic and Kaula*, 1995] and nonlinear viscosity [e.g., *Houseman and Molnar*, 1997; *Molnar et al.*, 1998] can significantly alter the growth rates of Rayleigh-Taylor instabilities. In addition, the timescale and character of these viscous perturbations can be influenced by symmetric horizontal shortening of the lithosphere [e.g., *Conrad and Molnar*, 1997; *Molnar et al.*, 1998] and the presence of an overlying crust [e.g., *Neil and Houseman*, 1999; *Houseman et al.*, 2000]. The explicit assumption of these models is that during convergence the underlying mantle lithosphere undergoes homogeneous, distributed thickening beneath the evolving orogen (e.g., Figure 1a).

[5] An alternate hypothesis suggests that in some cases the mantle lithosphere at continental plate collision may be accommodated by underthrusting/subduction of one plate beneath the other along a narrow shear zone (Figure 1b). The concept of subduction-style behavior of the mantle lithosphere has been incorporated as a basal boundary condition to drive crustal-scale models of compressional orogens [e.g., *Willett et al.*, 1993; *Beaumont et al.*, 1996].

These studies demonstrate that for certain tectonic regimes a mantle subduction basal boundary condition is favored over a distributed Rayleigh-Taylor-type instability of the mantle lithosphere as the former produces a distinct asymmetry in the crustal deformation which is observed in many small collisional orogens.

[6] Recent results from upper mantle scale numerical models of continental plate convergence demonstrate that it may not be necessary to be restricted to either of these “end-member” styles of deformation [*Pysklywec et al.*, 2000]. The models exhibit several modes of mantle lithosphere deformation including subduction-style underthrusting, ablative plate consumption, and slab breakoff, as well as Rayleigh-Taylor gravitational instability. Most notably, these modes were not necessarily independent but often occurred contemporaneously or sequentially through various stages of the model evolution. While this work may provide insight into the behavior of the mantle lithosphere during orogenesis, it was restricted to nontemperature-dependent viscoplastic rheologies, only considered the sensitivity of the models to selected parameters and focused on the late stage evolution of the system.

[7] In this study we build on the preliminary work to examine the evolution of the lithosphere (i.e., crust, but especially the mantle lithosphere) during the initial development of an orogenic event. The numerical model has been enhanced to treat thermal conduction and advection in the system and includes temperature dependence in material parameters such as rheology and density. By conducting a range of computational experiments of continental plate convergence we will attempt to identify the preferred style of deformation of the mantle lithosphere under what may be Earth-like conditions of continental collision. In particular, we investigate the conditions that determine what fraction of the mantle lithosphere deforms by distributed, Rayleigh-Taylor viscous thickening (Figure 1a) and/or subduction-style underthrusting of one plate beneath the other (Figure 1b).

[8] As a case study, the numerical results are considered in the context of the evolution of the lithosphere of South Island, New Zealand. The oblique continent-continent convergence between the Pacific and Australian plates in the region is responsible for the development of the continental collision zone and the Southern Alps, but the current process of deformation in the underlying mantle lithosphere is still ambiguous [e.g., *Beaumont et al.*, 1996; *Molnar et al.*, 1999]. While we focus on the example of South Island, New Zealand, the results of the numerical experiments may also have general implications for development of the lithosphere in association with other young orogens, as well as for older, larger-scale collisional events.

## 2. Description of the Numerical Model

[9] The numerical model uses arbitrary Lagrangian-Eulerian (ALE) finite element techniques to solve for the plane strain deformation of viscoplastic materials [*Fullsack*, 1995]. The creeping flows associated with the geodynamic models are characterized by extremely high Prandtl numbers ( $Pr$ , where  $Pr = \nu/\kappa$ ;  $\nu$  is kinematic viscosity and  $\kappa$  is thermal diffusivity), and therefore inertial forces may be neglected in the system. Furthermore, we consider the case

of incompressible flow. With these assumptions the governing thermomechanical equations for the numerical model include the conservation equations of momentum, mass, and internal energy [e.g., *Landau and Lifshitz*, 1959]:

$$\nabla \cdot (\rho \mathbf{u}) = 0, \quad (1)$$

$$\nabla \cdot \sigma_{ij} + \rho g = 0, \quad (2)$$

$$\rho c_p \left( \frac{\partial T}{\partial t} + \mathbf{u} \cdot \nabla T \right) = k \nabla^2 T + \rho H. \quad (3)$$

This system of equations is completed by an associated linearized equation of state:

$$\rho = \rho_0 [1 - \alpha(T - T_0)]. \quad (4)$$

In equations (1)–(4),  $\rho$ ,  $\mathbf{u}$ , and  $T$  represent the fields of density, velocity, and temperature, respectively. The variables  $g$ ,  $c_p$ ,  $\alpha$ ,  $k$ ,  $H$ , and  $t$  are gravitational acceleration, heat capacity, thermal expansivity, thermal conductivity, rate of internal heat production per unit mass, and time. The stress tensor,  $\sigma_{ij}$ , may be divided into two components:

$$\sigma_{ij} = \sigma'_{ij} - p \delta_{ij}, \quad (5)$$

where  $\sigma'_{ij}$  is the deviatoric stress tensor and  $p$  is the pressure (where for an incompressible fluid,  $p = -\frac{1}{3} \sigma_{ii}$ ).

[10] In the viscoplastic numerical model the deviatoric stress is determined at each computational node as the lesser value of either a yield stress  $\sigma_y$  or viscous stress  $\sigma_v$ ; i.e.,  $\sigma'_{ij} = \min(\sigma_y, \sigma_v)$ . For the frictional plastic yield stress a Drucker-Prager yield criterion is used, which is equivalent to the Coulomb criterion in plane strain [*Fallsack*, 1995]:

$$\sigma_y = p \sin \phi + c_0. \quad (6)$$

In this expression  $\phi$  and  $c_0$  represent the internal angle of friction and the cohesion, respectively; the flow law is nonassociative because the deformation is incompressible. The viscous stress is defined as

$$\sigma_v = 2\eta_e \dot{\epsilon}, \quad (7)$$

where, for power law creep, the effective viscosity  $\eta_e$  is

$$\eta_e(\dot{\epsilon}, T) = \left( 3^{\frac{-(n+1)}{2n}} 2^{\frac{1-n}{n}} \right) A^{\frac{1}{n}} \dot{\epsilon}^{\frac{1}{n}-1} e^{\frac{Q}{nRT}} \quad (8)$$

and  $\dot{\epsilon}$  is the strain rate. The variables  $A$ ,  $n$ , and  $Q$  are the viscosity parameter, power exponent, and activation energy from uniaxial laboratory experiments, and  $R$  is the ideal gas constant. (Note that the first bracketed term on the right-hand side of equation (8) is necessary for the conversion of the uniaxial laboratory experimental data to a state of stress that is independent of the choice of coordinate system.) The accuracy of the computational code has been verified by an extensive series of benchmarking tests. For example, detailed analyses of the growth of Rayleigh-Taylor instabilities indicate that our numerical formulation is in close agreement with other numerical and analytical studies [e.g., *Houseman and Molnar*, 1997; *van Keken et al.*, 1997].

[11] Figure 2 illustrates the initial geometry of the models. The solution space is divided into five separate regions. At the top, region 1 is a crustal layer; regions 2 and 3 comprise the uppermost mantle; region 4 is a small weak block that serves to locate initial deformation in the model; and region 5 is the sublithospheric upper mantle. The numerical resolution is significantly higher in the upper portion of the model in order to better resolve the lithospheric deformation that develops in the experiments. As indicated in Figure 2, half of the total computational nodes are concentrated in the top quarter of the box.

[12] Creeping motion in the model is driven by a combination of buoyancy forces (arising from thermal and inherent chemical density variations) and plate motions imposed at the boundary. The latter are simulated in the model by introducing new lithosphere into the box at a horizontal velocity  $v_x = 1.5 \text{ cm yr}^{-1}$  at the right boundary of the model (Figure 2a). The left margin of the lithosphere is held fixed, and a small outward flux,  $v_{xb}$  is distributed evenly along the sides of the sublithospheric upper mantle to balance the mass of injected lithosphere. The models are designed to consider an intracratonic style collision and disregard the influence of any precursor phase of oceanic subduction.

[13] The solution space has a free top surface and zero tangential stress (“free slip”) along all four sides. Material is not permitted to penetrate the lower boundary of the box. This condition is not overly restrictive because we limit our investigations to the early stages of the collisional models when the influence of the bottom boundary on the deformation of the lithosphere is minimal.

[14] To facilitate interpretation of results of the numerical experiments, we define a “reference model,” EX1, as described in Table 1. Parameters that are not spatially, thermally, or temporally dependent in the model are also listed in Table 1.

[15] The power law viscous parameters given for region 1 in Table 1 are based on experimental results for wet quartzite [*Gleason and Tullis*, 1995]. In our numerical models we further scale down the effective viscosity of region 1 by a factor of 0.25 in order to allow the lowermost crust to weaken sufficiently and develop some degree of crustal detachment from the underlying mantle. The chosen factor of 0.25 is somewhat arbitrary (being derived from observation of a series of numerical models), but it may be reasonable given the relatively high uncertainty in constraining wet material rheologies at depth, particularly the range of measured  $A$  values (equation (8)), the approximation of a purely quartzite controlled rheology, and the associated uncertainties in lithospheric temperatures.

[16] The physical parameters of regions 2, 3, and 5 are exactly the same in the model (see Table 1), thus representing a compositionally homogeneous mantle. In the numerical experiments, however, it will be demonstrated that there is significant rheological differentiation of the mantle as a result of spatial and dynamic variations (e.g., in temperature, strain, and strain rate) in the system. The parameters used to define power law creep in the mantle are derived from the experimental results of *Chopra and Paterson* [1984] for wet Åheim dunite (Table 1). In experiments subsequent to the reference model we adopt different olivine flow laws from this one in order to determine the sensitivity of the model to alternative mantle

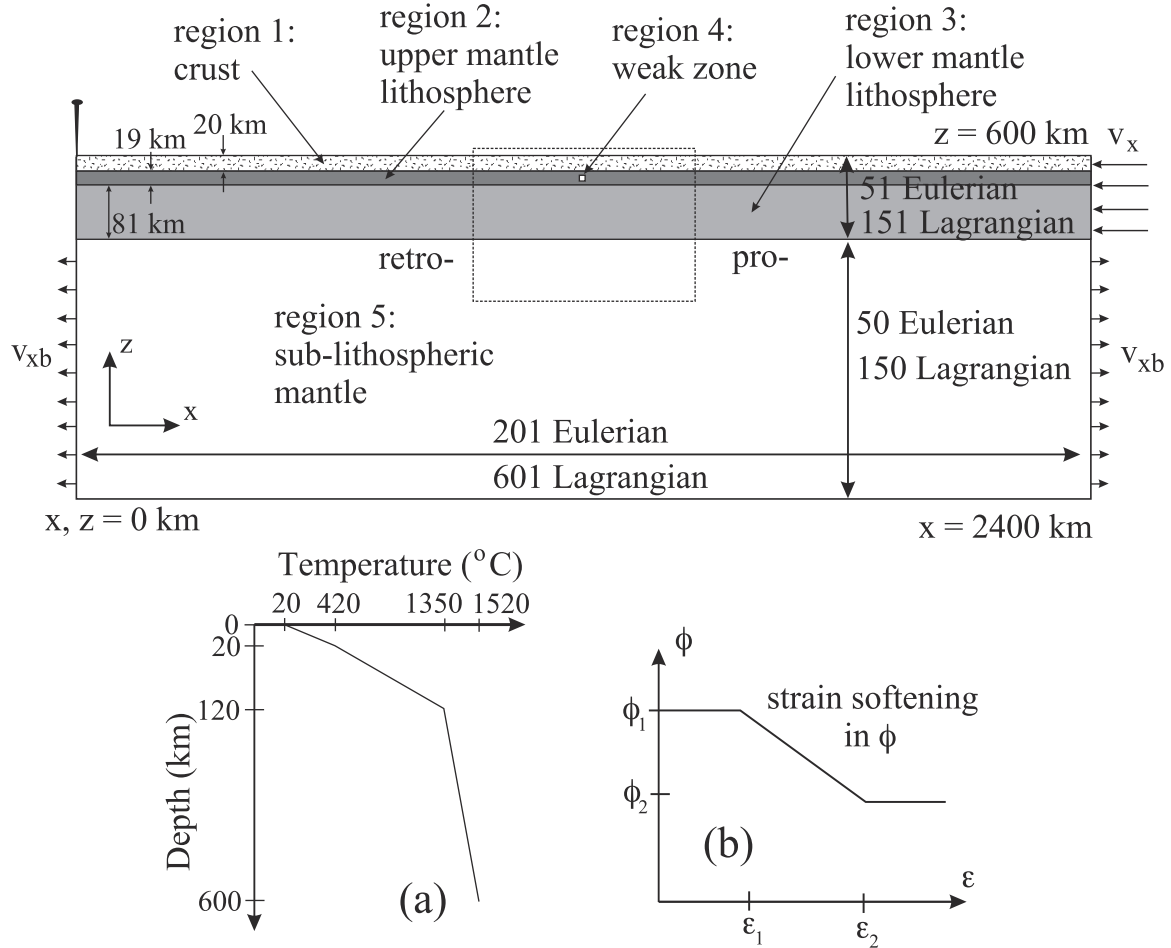


**Figure 2.** (a) Illustration of the initial configuration for the numerical numerical experiments. The separate regions which define the model are denoted and the corresponding physical parameters are described in Table 1. The number of node points in the horizontal and vertical directions for the Eulerian and Lagrangian grids indicates resolution for the finite element mesh of quadrilateral elements. Continental convergence is incorporated by introducing new lithosphere at the right boundary of box with velocity  $v_x$ , while the left margin of the lithosphere is held fixed and an outward balancing flux velocity,  $v_{xb}$  is distributed along sides of the sublithospheric mantle. The retro- and pro- sides of lithosphere are denoted, and a dashed box depicts approximate portion of the full solution space that is shown in Figures 3–12. (b) Initial variation in temperature with depth. (b) Change in internal angle of friction  $\phi$  with accumulated strain  $\epsilon$ .

rheologies. It is important to note that because the mantle material is chemically homogeneous, it is difficult to determine a strict division between the lithosphere and sublithospheric mantle. However, to aid in our description of the numerical experiments, we will refer to material

initially at <120 km depth and cooler than 1350°C (i.e., material in the numerical high-resolution region) as the lithosphere. Thus the mantle lithosphere comprises the region above the bottom of this lithosphere and below the base of the crust (Figure 2a).

**Table 1.** Physical Parameters for Reference Model EX1<sup>a</sup>

Region	Plasticity					Viscosity				Density		
	$c_0$ , Pa	$\phi_1$	$\phi_2$	$\epsilon_1$	$\epsilon_2$	$A$ , $\text{Pa} \cdot \text{s}^{-n}$	$Q$ , $\text{kJ mol}^{-1}$	$n$	Ref	$\rho_0$ , $\text{kg m}^{-3}$	$T_0$ , K	$\alpha$ , $\text{K}^{-1}$
1	$10^7$	$15^\circ$	$15^\circ$	—	—	$1.1 \times 10^{-28}$	223	4.0	1	2800	500	$3.0 \times 10^{-5}$
2	0	$15^\circ$	$2^\circ$	0.5	1.5	$5.495 \times 10^{-25}$	498	4.48	2	3300	750	$2.0 \times 10^{-5}$
3	0	$15^\circ$	$2^\circ$	0.5	1.5	$5.495 \times 10^{-25}$	498	4.48	2	3300	750	$2.0 \times 10^{-5}$
4	$10^7$	0	0	—	—	$5.495 \times 10^{-25}$	498	4.48	2	3300	750	$2.0 \times 10^{-5}$
5	0	$15^\circ$	$2^\circ$	0.5	1.5	$5.495 \times 10^{-25}$	498	4.48	2	3300	750	$2.0 \times 10^{-5}$

<sup>a</sup>References for viscosity parameters: 1, wet quartzite, *Gleason and Tullis* [1995]; 2, wet Åheim dunite, *Chopra and Paterson* [1984]. Physical constants in the models are  $g = 10.0 \text{ m s}^{-2}$ ,  $c_p = 750 \text{ J kg}^{-1} \text{ K}^{-1}$ ,  $H = 0 \text{ W m}^{-1} \text{ K}^{-1}$ ,  $\kappa = 1.0 \times 10^{-6} \text{ m}^2 \text{ s}^{-1}$ , and  $R = 8.31 \text{ J mol}^{-1} \text{ K}^{-1}$ .



**Table 2.** List of Numerical Experiments

Experiment	Description-Variation From Reference Model
EX1	reference model
EX2	wet olivine mantle <sup>a</sup> $A = 4.89 \times 10^{-15} \text{ Pa}^{-n} \text{ s}^{-1}$ , $n = 3.5$ , $Q = 515 \text{ kJ mol}^{-1}$ in regions 2, 3, 4, 5
EX3	dry olivine mantle <sup>a</sup> $A = 4.85 \times 10^{-17} \text{ Pa}^{-n} \text{ s}^{-1}$ , $n = 3.5$ , $Q = 535 \text{ kJ mol}^{-1}$ in regions 2, 3, 4, 5
EX4	increase range of strain for plastic softening $\epsilon_1 = 0.5 \rightarrow \epsilon_2 = 5.0$ (for same $\phi_1 = 15^\circ$ and $\phi_2 = 2^\circ$ )
EX5	suppress strain softening set $\phi_1 = 15^\circ$ and $\phi_2 = 15^\circ$
EX6	increase initial geotherm in model (see text)
EX7	increase crustal thickness to $\sim 40.8 \text{ km}$
EX8	make mantle neutrally buoyant by setting $\alpha = 0$ in all regions
EX9	decrease imposed convergence velocity to $v_x = 0.5 \text{ cm yr}^{-1}$
EX10	increase imposed convergence velocity to $v_x = 4.5 \text{ cm yr}^{-1}$

<sup>a</sup>References for viscosity parameters 1, *Hirth and Kohlstedt* [1996].

[17] The initial geotherm for the experiments (Figure 2b) is laterally uniform and is defined by a fixed surface temperature of  $20^\circ\text{C}$  and a series of underlying linear gradient segments to the bottom of the solution space: an increase to  $400^\circ\text{C}$  at the base of the crust, to  $1350^\circ\text{C}$  at a depth of  $120 \text{ km}$ , and to the bottom of the model where the temperature is constant at  $1520^\circ\text{C}$ .

[18] The frictional plastic rheology of the olivine constituent of the model is permitted to weaken over a prescribed range of accumulated strain  $\epsilon$  (see Table 1 and Figure 2c). We introduce this as an arbitrary mechanism of strain softening in the mantle lithosphere [e.g., *Poirier*, 1980; *Visser et al.*, 1995; *Jin et al.*, 1998; *Braun et al.*, 1999]. Incorporating the ability of the model to self-consistently strain soften and to localize strain may be an important agent for initializing and sustaining deformation during the collision of rigid lithospheric plates (e.g., *Pysklywec et al.* [2000]; see results below).

[19] A small block of weak material (of physical dimension  $10 \text{ km}$  by  $10 \text{ km}$ ) is inserted into the center of the upper mantle lithosphere, the strongest of the model layers, to seed the onset of deformation in the numerical model. The seed only influences the initial position of conjugate plastic failure planes, not the ensuing finite deformation. In similar experiments without this weak zone, convergence is accommodated by distributed thickening of the lithosphere across the entire length of the solution space or periodic buckling of the layers. The implicit assumption is that weak zones exist at plate boundaries.

[20] Using EX1 as a basis, we present a series of experiments in which various modeling parameters are changed incrementally (Table 2).

### 3. Model Results

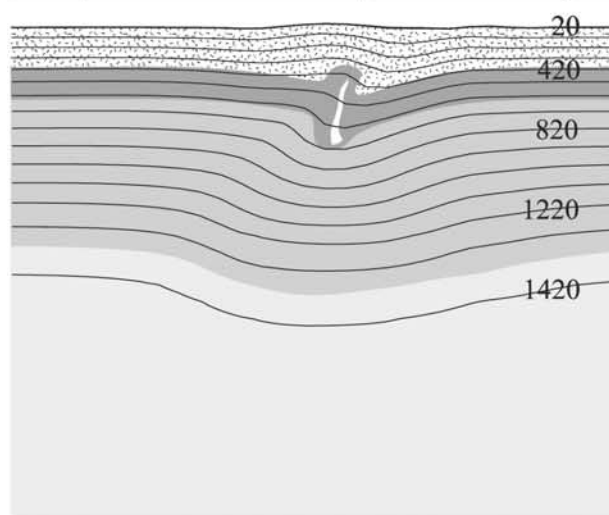
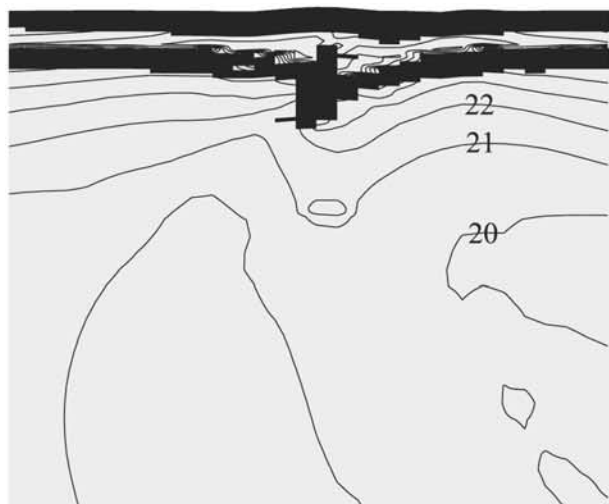
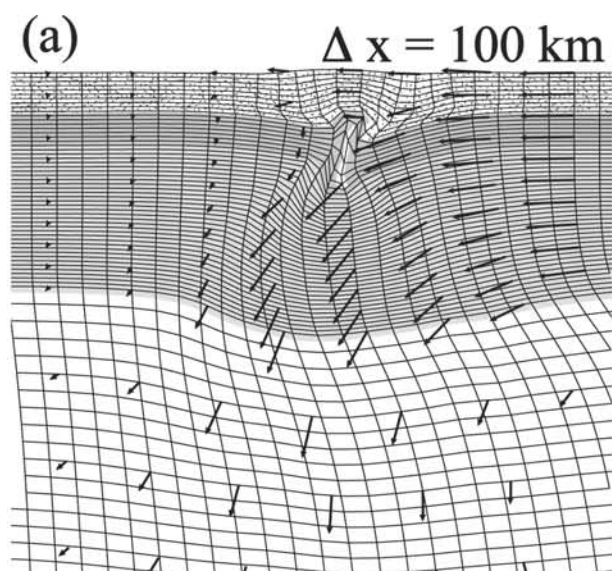
#### 3.1. Experiment EX1

[21] The reference model, EX1, is shown at four stages during its evolution, corresponding to increasing amounts of accumulated lithospheric convergence (Figure 3).

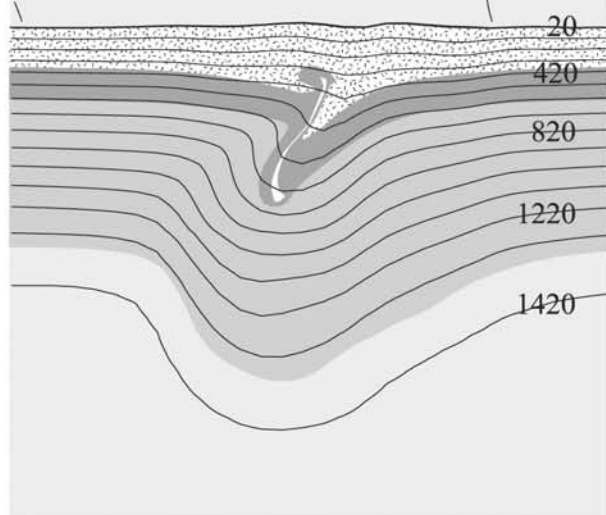
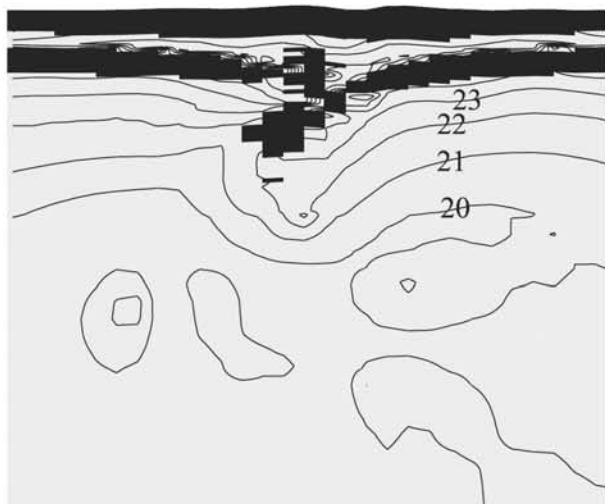
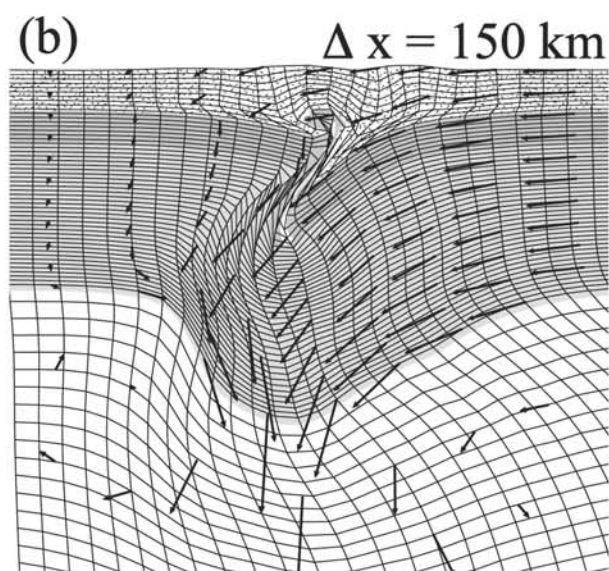
[22] In the earliest stages of convergence (not shown in Figure 3) the imposed convergence was taken up by a distributed thickening of the lithosphere along cross conjugate thrust zones at the weak seed in the strong frictional plastic upper mantle. One of these shear zones progressively becomes dominant as a consequence of the positive feedback of strain softening. At  $\Delta x = 100 \text{ km}$  (Figure 3a), the prolithosphere is beginning to underthrust at the collision

zone (where  $\Delta x$  denotes the accumulated imposed shortening of the lithosphere relative to initiation of the model). Deformation of the Lagrangian mesh indicates that this motion is largely accommodated along a diffuse shear zone in the upper mantle lithosphere. The map of the plastic and viscous domains illustrates the rheological divisions of the model lithosphere and sublithospheric mantle. The upper crust undergoes plastic deformation, and this layer is underlain by a ductile region in the lower crust where the higher temperatures decrease the viscous stress below the yield stress. Under these stress and temperature conditions the uppermost layer of the underlying olivine mantle lithosphere is in the plastic regime.

[23] By  $\Delta x = 150 \text{ km}$ , there is significant underthrusting of the proside of the mantle lithosphere beneath the retro-side at the collision zone along a well-developed shear zone (Figure 3b). This underthrusting/subduction-style mode of deformation of the upper mantle lithosphere is the mechanism conceptually illustrated in Figure 1b. The upper portion of the mantle lithosphere is essentially “plate-like” and is characterized by high plastic yield strength and high effective viscosity (e.g.,  $\eta_e$  reaching  $\sim 10^{24}$ – $10^{25} \text{ Pa s}$ ) rheologies. Deformation of the Lagrangian grid suggests that the plate-like region comprises approximately the top  $60$ – $70 \text{ km}$  of the mantle lithosphere. That is, there is little internal deformation of the Lagrangian mesh in the upper mantle lithosphere apart from bending, but there is evidence of increasing horizontal shear in the grid in the lower regions. At the top of the model, there is continued thickening of the crustal layer at the collision zone. During this stage the crustal thickness reaches a maximum of  $\sim 38 \text{ km}$ , and the surface topography is as high as  $\sim 2 \text{ km}$ . The crust is effectively detached from the underlying mantle lithosphere along basal shear zones extending  $\sim 80 \text{ km}$  proward and  $\sim 60 \text{ km}$  retoward from the center of the collision zone. This detachment zone develops dynamically during heating and corresponding weakening at depth in the thickened crust which has a viscous rheology based on wet quartzite. The isotherms in Figure 3b reflect closely the geometry of lithospheric thickening and indicate that advection of heat in the system dominates over thermal diffusion. This means that the “root” of mantle lithosphere remains relatively cool as it is thrust deeper into the mantle. The associated lateral density contrast between the surrounding mantle and dense lithospheric root results in gravitational instability of the lower lithosphere [e.g., *Houseman et al.*, 1981].

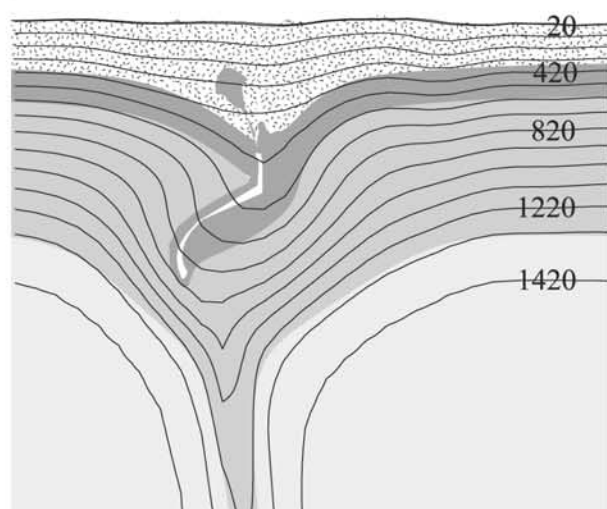
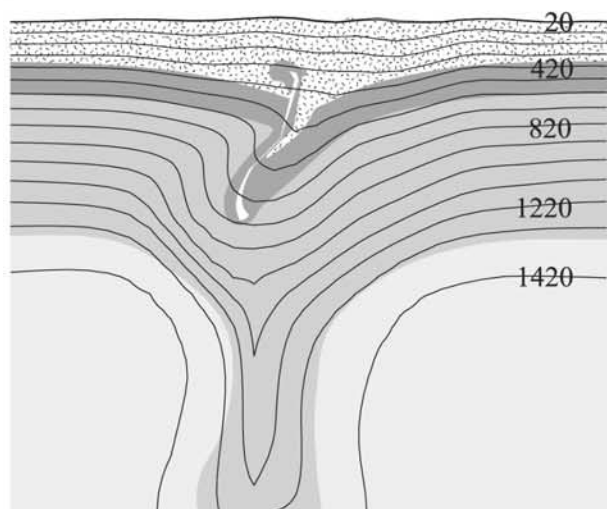
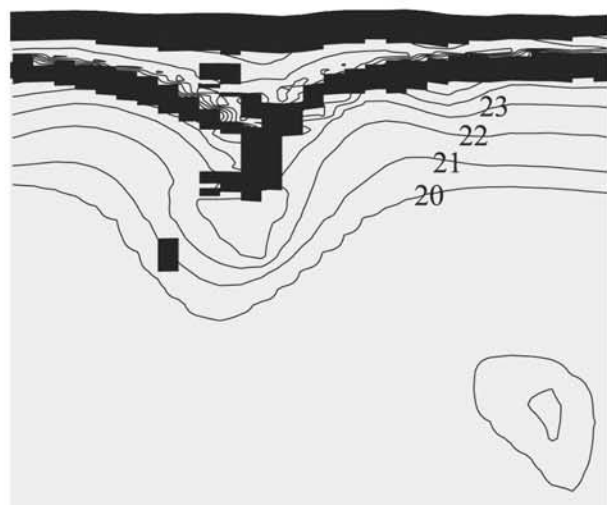
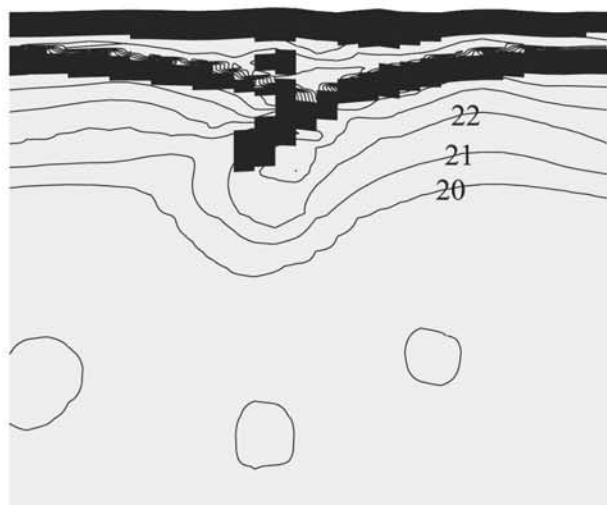
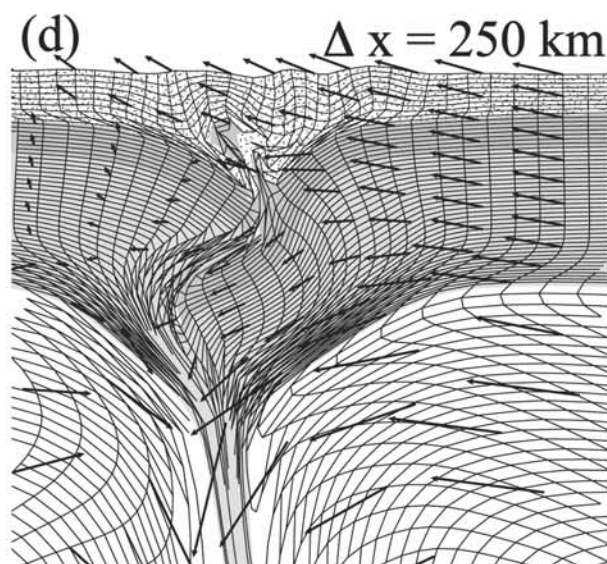
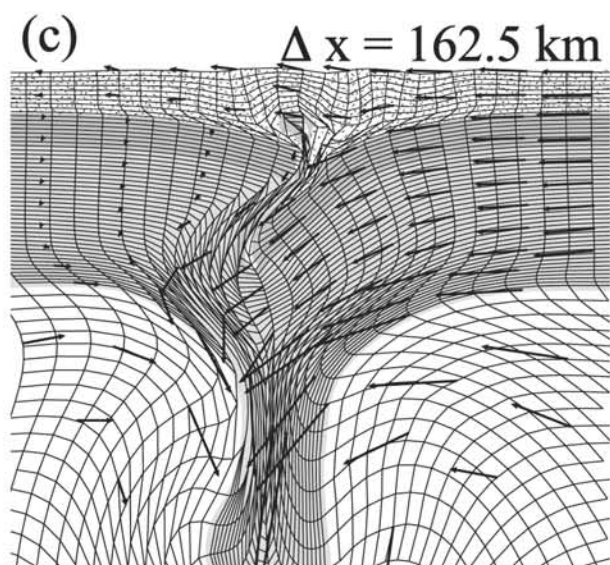


— 1.5 cm/yr



— 1.5 cm/yr





— 1.5 cm/yr

— 1.5 cm/yr

[24] Between  $\Delta x = 150$  and 162.5 km of convergence (Figures 3b and 3c) a Rayleigh-Taylor-type gravitational instability develops rapidly. In particular, the thickened lithospheric root is “dripping” at rates reaching  $\sim 5 \text{ cm yr}^{-1}$ , compared to the plate convergence velocity of  $1.5 \text{ cm yr}^{-1}$ . The upper region of the mantle lithosphere continues to behave in a plate-like manner. The underthrusting proplate, however, is starting to weaken (e.g., note deformation in Lagrangian grid, Figure 3c) where it is indented by the retroside. At this stage in the experiment it is difficult to define one specific deformational style for the system, but instead it may be characterized by contemporaneous, but distinct processes of crustal thickening, underthrusting/subduction of the upper plate-like portion of the mantle lithosphere and viscous instability of the lower lithosphere.

[25] The  $\Delta x = 200$  km stage of the model is dominated by vigorous flow in the sublithospheric mantle as the viscous instability drips away from the lithosphere and entrains surrounding material from beneath the collision zone (Figure 3d). Subduction-style collision in the upper mantle lithosphere continues, but there is a polarity reversal as the retroplate begins to underthrust the proplate (Figure 3d). A new shear zone develops in this orientation to accommodate the motion. The strong underthrusting retroplate and corresponding localized weak shear zone are clearly depicted in the Lagrangian mesh. The indenter retroplate has significantly damaged the proplate and eventually this will lead to break off/detachment of the subducting prolimb [e.g., *Pysklywec et al.*, 2000]. A similar style of subduction polarity reversal by slab break off has been invoked conceptually to explain certain tectonic settings [e.g., *Teng et al.*, 2000]. The current model illustrates quantitatively the manner by which this reversal process may occur. A thick crust reaching  $\sim 55$  km has developed in the immediate area of the collision zone. Undulations in surface topography, however, are progressively migrating both retroward and proward away from the center of the collision zone as crust thickens by detachment at the base of the crust.

### 3.2. Experiment EX2

[26] Experiment EX2 considers the corresponding case with an alternative olivine rheology. In all other respects, the model is identical to EX1, except that the wet olivine rheology (Table 2) of *Hirth and Kohlstedt* [1996] is used for regions 2, 3, and 5. Figure 4 shows results of the numerical experiment after 150 km of convergence. The primary difference from EX1 is related to the development of the viscous gravitational instability. The Hirth and Kohlstedt wet olivine rheology is weaker than the *Chopra and Paterson* [1984] wet Åheim dunite, and consequently, the

lithospheric drip forms over a shorter timescale (i.e., compare Figure 4 to Figure 3b). Furthermore, in Figure 4 the contours of effective viscosity are concentrated more closely near the top of the mantle lithosphere than in Figure 3b, indicating a lower viscosity lower mantle lithosphere with the wet olivine of EX2. These variations between the two models illustrate that uncertainties in experimentally derived results (e.g., in this case, the rheology of wet olivine) can have significant influence on the numerical models.

[27] The boundary between the low-viscosity mantle lithosphere and the upper plate-like mantle lithosphere is especially distinctive in this model. The Lagrangian grid, for example, indicates that there is relatively little deformation in the upper 45–50 km of the mantle lithosphere. This region, instead, underthrusts as a flexed but coherent slab beneath the rigid retroplate. The subduction occurs at a shallow angle and seems to progress more easily than the parallel subduction in EX1, probably due to the lower inhibiting mantle lithosphere viscosities encountered by the slab in EX2. While the geometry of underthrusting is clearly asymmetric, the Rayleigh-Taylor instability is quite symmetrical and occurs directly below the center of the collisional orogen (i.e., location of maximum thickening of crust).

### 3.3. Experiment EX3

[28] The results of a similar experiment, but with a dry olivine mantle rheology [*Hirth and Kohlstedt*, 1996] are shown in Figure 5. The model suggests that the dry olivine rheology is considerably more stable than the wet olivine mantle in EX1 (Figure 3) or EX2 (Figure 4); the mantle lithosphere is largely underthrusting as a flexed plate with relatively little internal deformation during the first 150 km of convergence. As in EX1 and EX2, the shear zone is well developed within the plastic upper portion of the mantle lithosphere. There is some evidence for the onset of viscous instability of the lower mantle lithosphere as a small amount of material is entrained toward the thickening lithospheric root. The growth of the instability, however, is slow, and except in the low-viscosity region near the base of the lithosphere the development of the root continues to be governed by the plate convergence (note velocity vectors). Furthermore, the underthrusting of the proplate is less steep than that in EX2. As a result, the geometry of the mantle lithosphere root is somewhat asymmetric, and it is offset  $\sim 30$  km from the region of maximum crustal thickening.

### 3.4. Experiment EX4

[29] In experiments EX4 and EX5 we consider variations in our parameterization of strain softening of the mantle. In

**Figure 3.** (opposite) Evolution of reference model at cumulative convergence  $\Delta x$  of (a) 100 km ( $\sim 6.3$  Myr of physical time), (b) 150 km ( $\sim 9.5$  Myr), (c) 162.5 km ( $\sim 10.2$  Myr), and (d) 200 km ( $\sim 12.6$  Myr). The top frame at each time step shows the material regions as differentially shaded zones (i.e., as labeled in Figure 2). Note that regions 2, 3, and 5 are chemically identical (see Table 1), but they are shaded differently to act as marker units. The Lagrangian mesh (initially composed of rectangular cells) at one third the actual resolution and velocity vectors are superimposed to show internal deformation and instantaneous material displacement rate of change, respectively. The middle frame shades in dark the material in the plastic regime and denotes with light shading viscous material. On top of this plastic/viscous map, contours for log of effective viscosity  $\log(\eta_e)$  are plotted at intervals of one. The bottom frame repeats the material fields, but contours of temperature have been superimposed; contour interval is  $100^\circ\text{C}$ , starting at  $20^\circ\text{C}$  at the surface. Only a portion of the full numerical solution space is shown (see Figure 2).



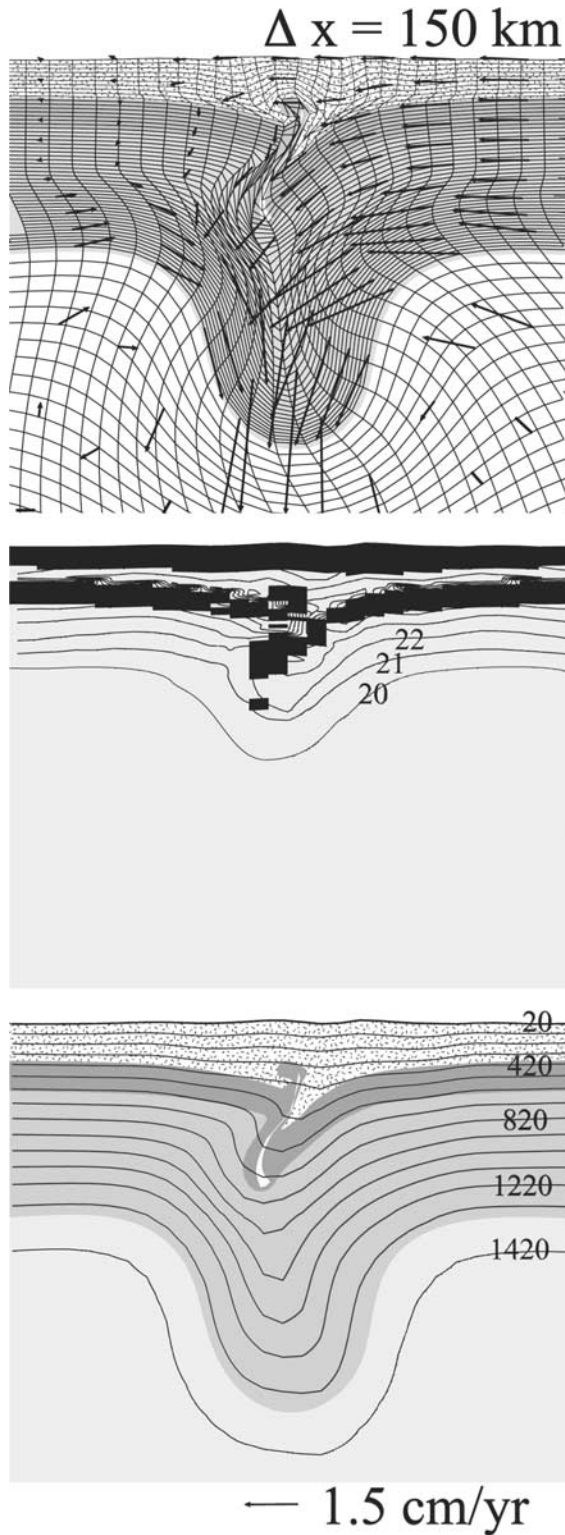


**Figure 4.** Evolution of EX2 at cumulative convergence  $\Delta x = 150 \text{ km}$  ( $\sim 9.5 \text{ Myr}$ ). Same as reference model EX1, but *Hirth and Kohlstedt* [1996] wet olivine rheology power law creep is used for regions 2, 3, and 5 (see Table 2). (top) Material regions, Lagrangian mesh, and velocity vectors; (middle) plastic/viscous map and isotherms; and (bottom) repeat of material regions and plot of log of effective viscosity (refer to Figure 3 for details).

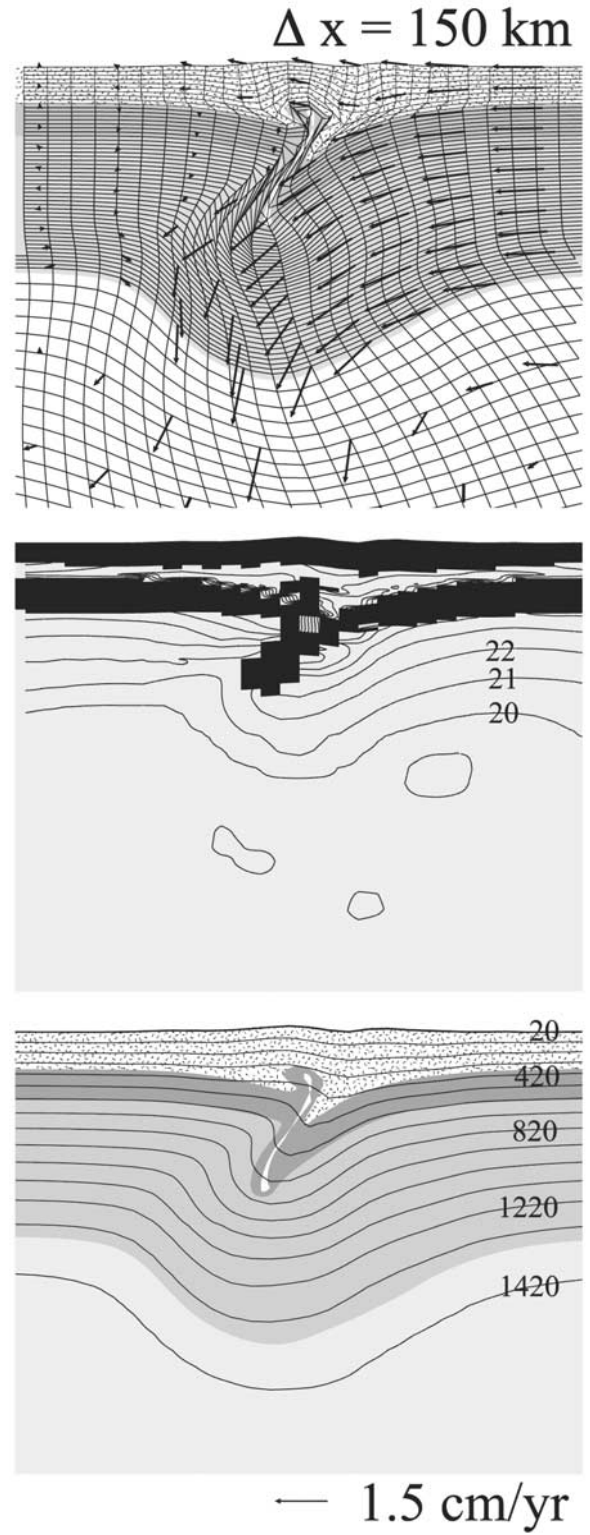


**Figure 5.** Evolution of EX3 at cumulative convergence  $\Delta x = 150 \text{ km}$  ( $\sim 9.5 \text{ Myr}$ ). Same as reference model EX1, but *Hirth and Kohlstedt* [1996] dry olivine rheology power law creep is used for regions 2, 3, and 5 (see Table 2). (top) Material regions, Lagrangian mesh, and velocity vectors; (middle) plastic/viscous map and isotherms; and (bottom) repeat of material regions and plot of log of effective viscosity (refer to Figure 3 for details).

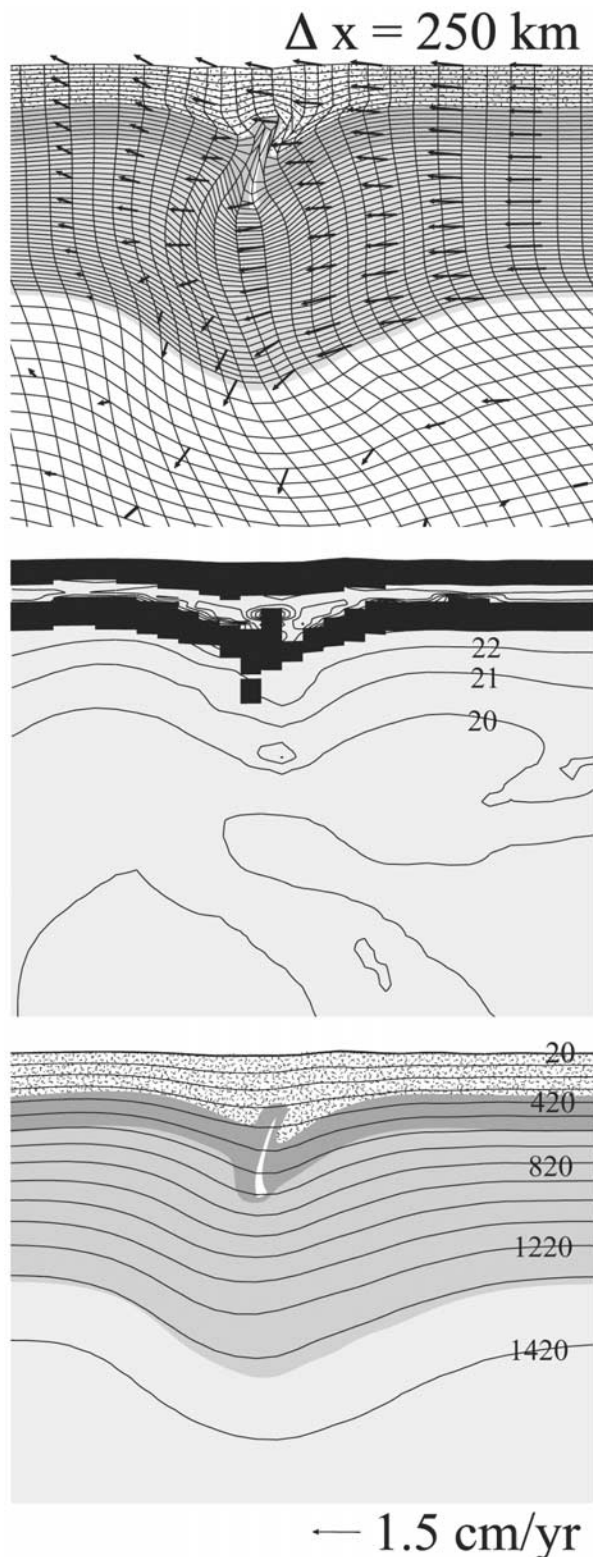


**Figure 6.** Evolution of EX4 at cumulative convergence  $\Delta x = 250$  km ( $\sim 15.8$  Myr). Same as reference model EX1, but strain softening occurs over larger interval in regions 2 and 5 (see Table 2). (top) Material regions, Lagrangian mesh, and velocity vectors; (middle) plastic/viscous map and isotherms; and (bottom) repeat of material regions and plot of log of effective viscosity (refer to Figure 3 for details).

EX4 the model returns to the *Chopra and Paterson* [1984] wet Åheim dunite mantle rheology, but the strain softening occurs over a larger interval of strain ( $\epsilon_1 = 0.5$ ;  $\epsilon_2 = 5.0$ ) than in the preceding models ( $\epsilon_1 = 0.5$ ;  $\epsilon_2 = 1.5$ ). Figure 6 shows the results at a relatively high accumulated convergence of  $\Delta x = 250$  km. It should be emphasized that strain softening in the model will only be occurring in materials at plastic yield, i.e., approximately the uppermost 20 km of the mantle lithosphere (see Figure 6, plasticity map); there is no strain dependence in the power law creep, only strain rate dependence of viscosity. Otherwise, the rheology of the model is exactly the same as that prescribed for EX1. The most conspicuous difference between EX4 and the previous experiments is the reluctance of the lithosphere to underthrust. This is a result of the high upper limit in strain softening as, for example, the material must reach 500% strain before it achieves the weakest rheology at a given pressure. Furthermore, the pressure dependence of the Drucker-Prager frictional plasticity (equation (6)) results in increasing strength when the upper mantle is progressively buried, offsetting the weakening owing to strain softening. Consequently, it is difficult for a shear zone to develop in the mantle lithosphere (compare Lagrangian grid in Figure 6 to that of Figure 3b). In the absence of an accommodating “weak” shear between the plates, the collision zone between the promantle and retromantle lithosphere is essentially locked and becomes progressively stronger as it is pushed deeper by the imposed convergence. The overlying crust accumulates in this trough, reaching thicknesses of  $\sim 65$  km. A wide zone of lithospheric thickening has developed surrounding the main lithospheric root beneath the collision zone. The lower mantle lithosphere in the root is slowly beginning to develop a gravitational instability as shown by velocities that are approximately double the rate of imposed convergence.

### 3.5. Experiment EX5

[30] In experiment EX5 the materials do not strain soften at all (see Table 2). Figure 7 shows results from this experiment, again at a well advanced stage,  $\Delta x = 300$  km. Even with the presence of the weak seed in the upper mantle lithosphere, the model shows no propensity to underthrust because there is no longer a sufficient mechanism to permit localization of deformation. Instead, after some initial local deformation, convergence is accommodated by buckling (i.e., large-scale folding) and shortening of the lithosphere. The buckling is most prominent in the plastic region of the upper mantle lithosphere (e.g., refer to map of plasticity and Lagrangian mesh). The lower mantle lithosphere has thickened somewhat beneath this “locked collision zone,” but the initial amplitude represents a small instability. Consequently, the gravitational instability does not grow rapidly, even after this significant amount of convergence. The results of experiments EX4 and EX5 suggest that the onset of gravitational instability of the lower mantle lithosphere may require a sufficient (in both amplitude and timescale) agent of initial thickening to boost perturbations to instability over inhibiting factors (e.g., thermal diffusion, inherent viscous resistance). This is in agreement with other work relating to the development of lithospheric viscous instabilities [Conrad and Molnar, 1997; Houseman and Molnar, 1997; Molnar et al., 1998].



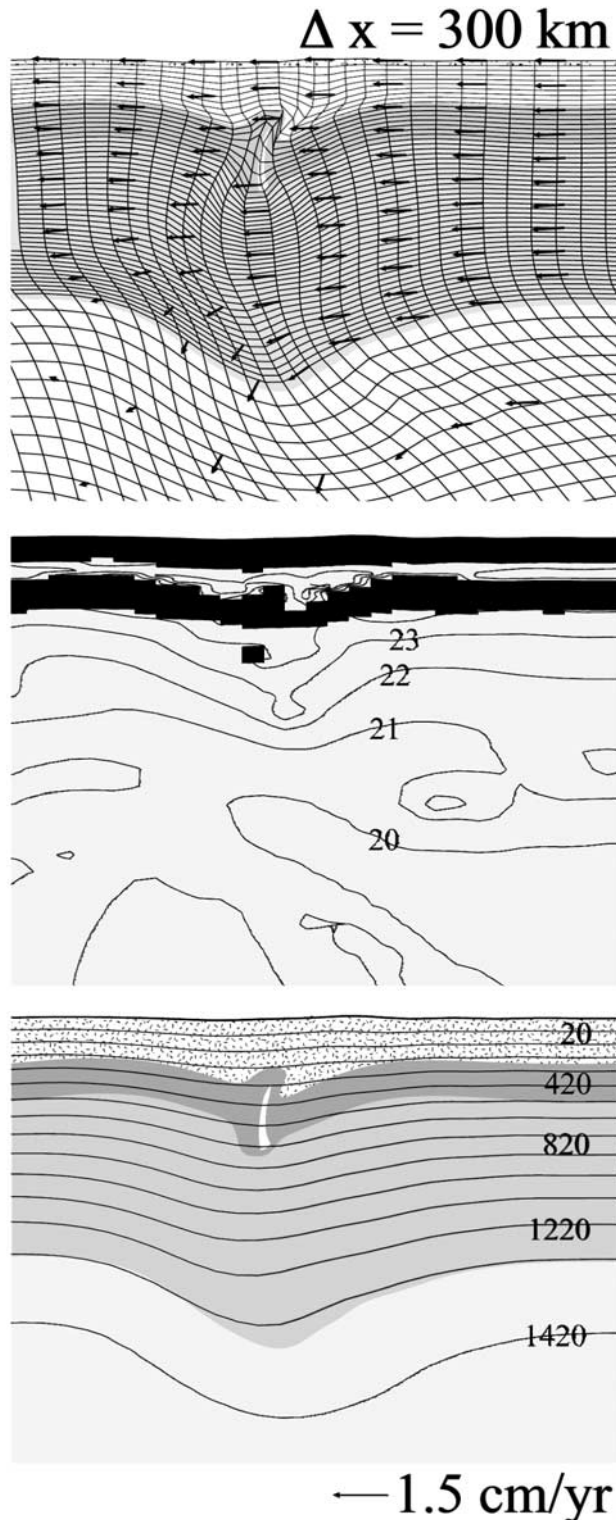


**Figure 7.** Evolution of EX5 at cumulative convergence  $\Delta x = 300$  km ( $\sim 19.0$  Myr). Same as reference model EX1, but strain softening is removed from the model (see Table 2). (top) Material regions, Lagrangian mesh, and velocity vectors; (middle) plastic/viscous map and isotherms; and (bottom) repeat of material regions and plot of log of effective viscosity (refer to Figure 3 for details).

The models EX1–EX3 indicate that underthrusting/subduction of the lithosphere may provide such a mechanism.

### 3.6. Experiment EX6

[31] Temperature plays an important role in determining the rheology and density of the materials in the model, and consequently, it is important in controlling the overall behavior of the system. In experiment EX6 we return to the same modeling parameters as in EX1 (Table 1) but arbitrarily increase the geotherm through the lithosphere by 11%, such that the temperature at the base of the lithosphere is now  $\sim 1525^\circ\text{C}$  as opposed to  $1350^\circ\text{C}$  in previous experiments. Even this subtle increase has a dramatic effect on the evolution of the system. The higher lithospheric temperatures weaken the lower mantle lithosphere and result in a rapid Rayleigh-Taylor downwelling (e.g., with velocities reaching  $\sim 8$  cm  $\text{yr}^{-1}$ ) and widespread entrainment in the lower mantle lithosphere (Figure 8). This gravitational instability in the lower mantle develops on a significantly shorter timescale than in the other experiments. The downwelling is well formed by  $\Delta x = 125$  km in EX6, whereas the lithospheric root in the reference model EX1 is relatively stable up to  $\sim 150$  km of convergence. These results demonstrate the strong sensitivity of the growth rate of viscous instabilities to the ambient temperature of the lithosphere. The high temperatures in the model also place more of the upper mantle lithosphere into the viscous regime and result in a thinner layer of plastic mantle lithosphere (Figure 8). Nevertheless, strain softening in this region localizes deformation between the colliding plates, and convergence of the lithosphere is accommodated by underthrusting of the upper plate-like region along a shear zone. However, the polarity of the “subduction” zone is reversed. In this case the former retroplate underthrusts the proplate in EX6. On the basis of these and other similar numerical experiments we observe that either of the initial pair of cross-conjugate failure planes in the plastic mantle lithosphere may become dominant in a given set of models. The increased lithospheric temperature in EX6 has apparently shifted the system away from the physical conditions which consistently chose that the proplate underthrust the retroplate at the first stages of development of the shear zone. In future experiments we hope to focus on this issue in order to achieve a better understanding of the process of the onset of localization, which may either be determined numerically or have a physical basis. Currently, we do not consider the polarity chosen to have particular significance.

### 3.7. Experiment EX7

[32] In experiment EX7 we test the sensitivity of a model with no upper mantle localization to the influence of a finite width lithospheric mantle weak zone, a possible representation of an inherited transcurrent boundary. The crustal thickness is doubled to 40.8 km, but the initial geotherm is the same (i.e., as in EX1) and the total lithospheric thickness remains at 120 km. This results in higher temperatures at the (now deeper) top of the mantle lithosphere, and consequently, this region is almost completely within the viscous regime. We increase the size of the weak zone by widening it to 20 km and extending it to the base of the lithosphere, e.g., to model a finite weak zone, such as a preexisting transcurrent plate boundary. Even with this



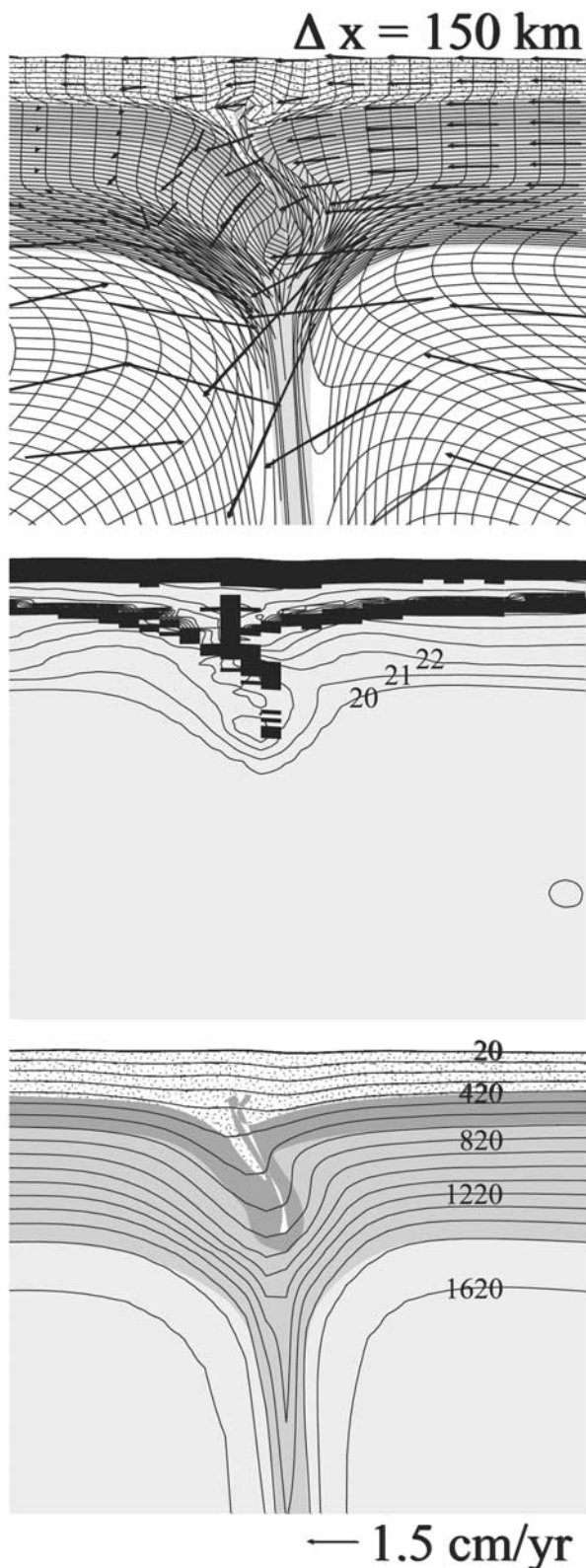


**Figure 8.** Evolution of EX6 at cumulative convergence  $\Delta x = 125$  km ( $\sim 7.9$  Myr). Same as reference model EX1, but lithospheric geotherm has been increased (see Table 2). (top) Material regions, Lagrangian mesh, and velocity vectors; (middle) plastic/viscous map and isotherms; and (bottom) repeat of material regions and plot of log of effective viscosity (refer to Figure 3 for details).

weakness, as illustrated in Figure 9, a relatively large amount of imposed convergence,  $\Delta x = 500$  km, is required to achieve modest deformation at the collision zone. The focused lithospheric deformation here is accompanied by distributed homogeneous thickening across a wider region than the plate collision zone.

[33] A viscous gravitational instability characterizes deformation in the lower portion of the lithosphere, as the lithospheric root drips into the mantle. In comparison to previous models (namely, EX1 and EX2) the viscous perturbation is quite small, and not a large amount of the surrounding lower mantle lithosphere is entrained toward the downwelling. This may partially be due to the effects of thermal diffusion in reducing the magnitude of the gravitational instability over the relatively large timescale of this experiment ( $\sim 32$  Myr). The upper mantle lithosphere is a strong viscous fluid, but since deformation cannot readily localize, it does not accommodate convergence by the coherent underthrusting of one plate beneath another along a shear zone. Instead, the retroplate and proplate collide in a form of ablative subduction [Tao and O'Connell, 1992] as both sides are consumed at the collision zone. With continued convergence the twin plates are pushed deeper into the mantle, and the contact zone migrates in the retroward direction [e.g., Pysklywec et al., 2000].

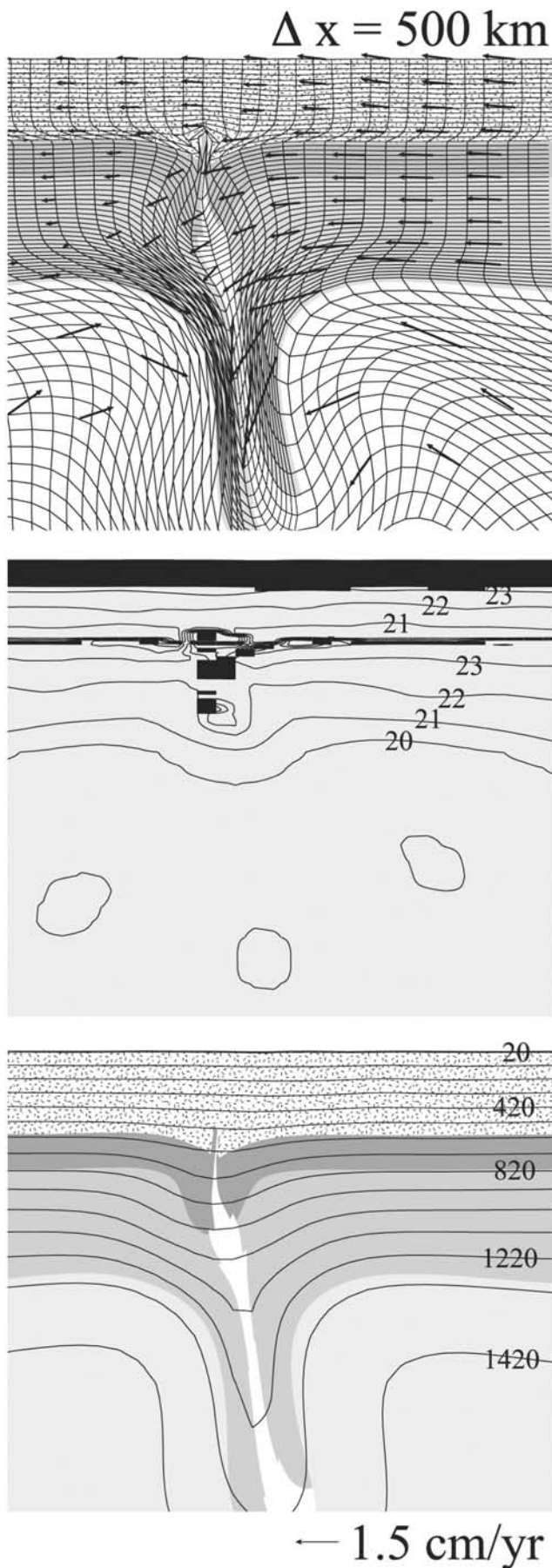
[34] For a “proto-EX7” experiment a small weak seed (e.g., as in EX1) was used instead of the finite weak zone of EX7. In this case the weak seed was not sufficient to focus deformation in the strong viscous lithosphere and the model deformed by homogeneous distributed thickening. This should not be interpreted to imply that the natural behavior would be the same because possible mechanisms of ductile strain localization are not considered in these models.

### 3.8. Experiment EX8

[35] To consider the evolution of a system with neutral buoyancy in the mantle lithosphere and sublithospheric mantle, we set  $\alpha = 0$  in all regions for EX8 (Figure 10). Thus the crust is defined by a constant density of  $2800 \text{ kg m}^{-3}$ , while all subcrustal material is fixed at  $3300 \text{ kg m}^{-3}$ . As in the reference model EX1, a shear zone develops in the upper mantle lithosphere, and this permits the proplate to underthrust the retroplate in a subduction-like manner. The perturbation of the lower mantle lithosphere, however, remains stable since it is no longer anomalously dense in relation to the surrounding sublithospheric mantle. Differences between EX8 and EX1 are therefore indicative of the importance of the development of the Rayleigh-Taylor instability. It is clear that the lower lithosphere behavior is quite different, but the underthrusting of the upper mantle lithosphere is similar. In later stages of the model the underthrusting/subduction mode of deformation, of course, remains dominant over any viscous instability of the mantle lithosphere.

### 3.9. Experiment EX9

[36] In all of the previous experiments a velocity of  $1.5 \text{ cm yr}^{-1}$  was applied as a plate convergence rate. For model EX9 the original setup (i.e., of reference model EX1) has been adopted, but the model is repeated with a lower convergence velocity of  $0.5 \text{ cm yr}^{-1}$ . Figure 11 shows the state of the model after 150 km of lithospheric convergence.



In this case with slow plate convergence the gravitational instability develops in advance of significant underthrusting because there is sufficient time for the viscous drip to evolve (i.e., EX9 has evolved for 28.5 Myr, whereas EX1 at  $\Delta x = 150$  km has taken only 9.5 Myr). By 150 km convergence in EX9 the lower part of the mantle lithosphere has dripped away into the sublithospheric mantle. A smaller portion of the lithosphere is removed compared to EX1 (Figure 3b) most likely because the initial unstable lithospheric root in EX9 is smaller than the corresponding thickening driven by rapid convergence in EX1. In later stages of the model the underthrusting/subduction mode remains relatively stable, as opposed to the other experiments where we observed slab detachment and a reversal of underthrust polarity. Therefore, despite the initial transient viscous instability, the system is characterized by a longer timescale underthrusting/subduction mode.

### 3.10. Experiment EX10

[37] In EX10 the convergence velocity that is imposed is triple the value from the reference model (i.e., now  $4.5 \text{ cm yr}^{-1}$ ), and Figure 12 shows the results of the experiment after 150 km of convergence which takes  $\sim 3.3$  Myr. Over this short timescale the underthrust/subduction mode of deformation is dominant in the model. The plate convergence causes the formation of a thickened lithospheric root, but the growth rate of the gravitational instability is less than the rate of subduction. For example, the velocity vectors at the bottom tip of thickened lithosphere is descending at  $\sim 3 \text{ cm yr}^{-1}$ , compared to the plate convergence of  $4.5 \text{ cm yr}^{-1}$ . As the model progresses, the lower lithosphere eventually drips away as in previous experiments, but through 150 km of rapid convergence, deformation of the mantle lithosphere is characterized by plate-like underthrusting.

## 4. A Case Study: Implications of Modeling Results for Lithospheric Deformation Across the Continental Collision Zone, South Island, New Zealand

[38] A prototypical example of small convergence continent-continent collision is the active tectonics of the continental collision zone of South Island, New Zealand (Figure 13). Although most of the displacement along the oblique collision is strike slip, there is an important component of plate convergence with a present magnitude  $\sim 1.0\text{--}1.3 \text{ cm yr}^{-1}$  [Walcott, 1998; Beavan *et al.*, 1999].

[39] The numerical experiments shown in section 3 were designed to relate approximately to the convergent component of the geodynamic configuration of South Island, New Zealand. The thickness of undeformed lithosphere (i.e., prior to tectonic thickening) in the region is  $\sim 120$  km of which the main continental crustal layer comprises  $\sim 20$  km

**Figure 9.** (opposite) Evolution of EX7 at cumulative convergence  $\Delta x = 500$  km ( $\sim 31.7$  Myr). Same as reference model EX1, but crust has been doubled in thickness to 40.8 km (see Table 2). (top) Material regions, Lagrangian mesh, and velocity vectors; (middle) plastic/viscous map and isotherms; and (bottom) repeat of material regions and plot of log of effective viscosity (refer to Figure 3 for details).



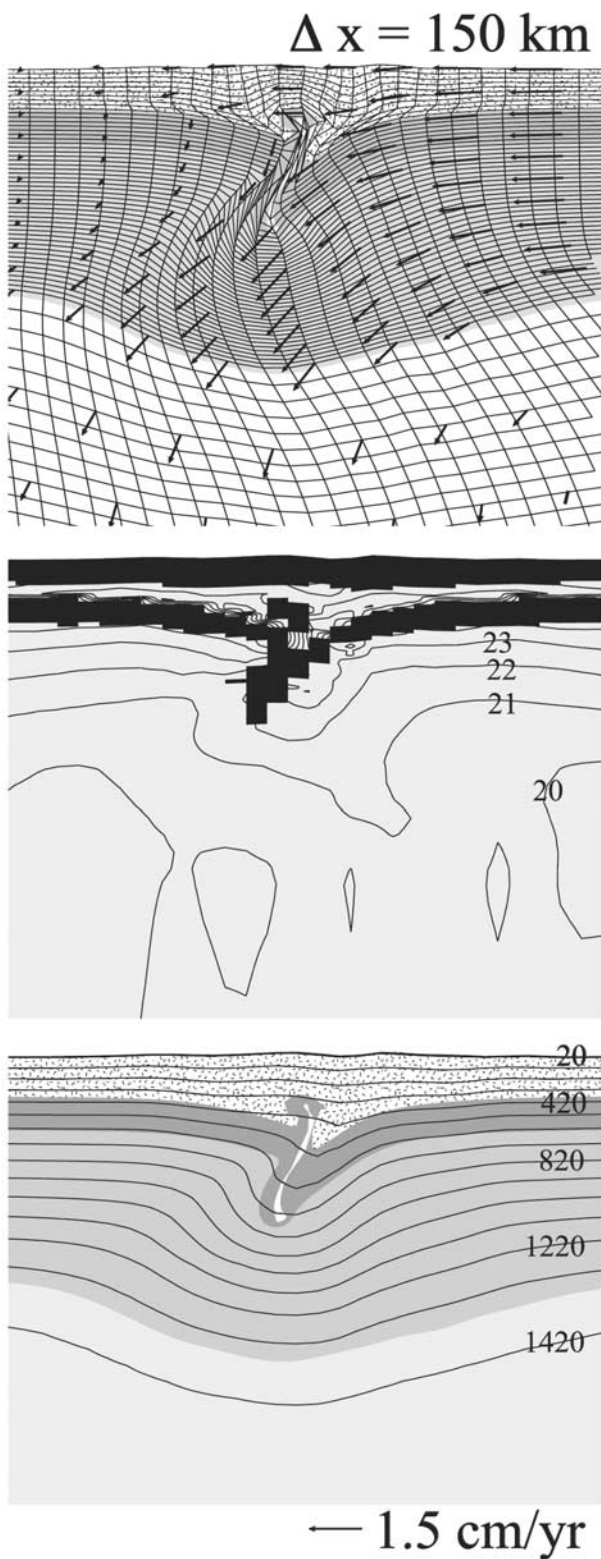


**Figure 10.** Evolution of EX8 at cumulative convergence  $\Delta x = 150 \text{ km}$  ( $\sim 9.5 \text{ Myr}$ ). Same as reference model EX1, but set  $\alpha = 0$  in all regions of model (see Table 2). (top) Material regions, Lagrangian mesh, and velocity vectors; (middle) plastic/viscous map and isotherms; and (bottom) repeat of material regions and plot of log of effective viscosity (refer to Figure 3 for details).

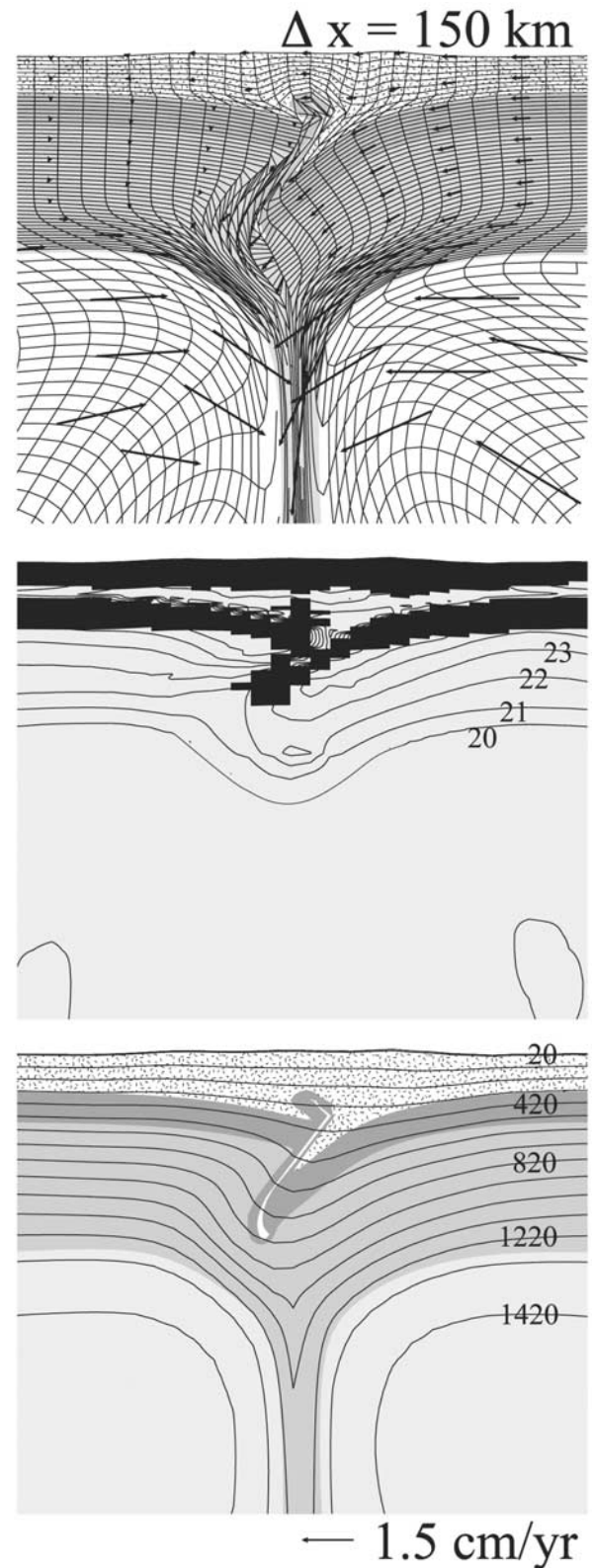


**Figure 11.** Evolution of EX9 at cumulative convergence  $\Delta x = 150 \text{ km}$  ( $\sim 28.5 \text{ Myr}$ ). Same as reference model EX1, but reduce imposed convergence rate to  $v_x = 0.5 \text{ cm yr}^{-1}$  (see Table 2). (top) Material regions, Lagrangian mesh, and velocity vectors; (middle) plastic/viscous map and isotherms; and (bottom) repeat of material regions and plot of log of effective viscosity (refer to Figure 3 for details).



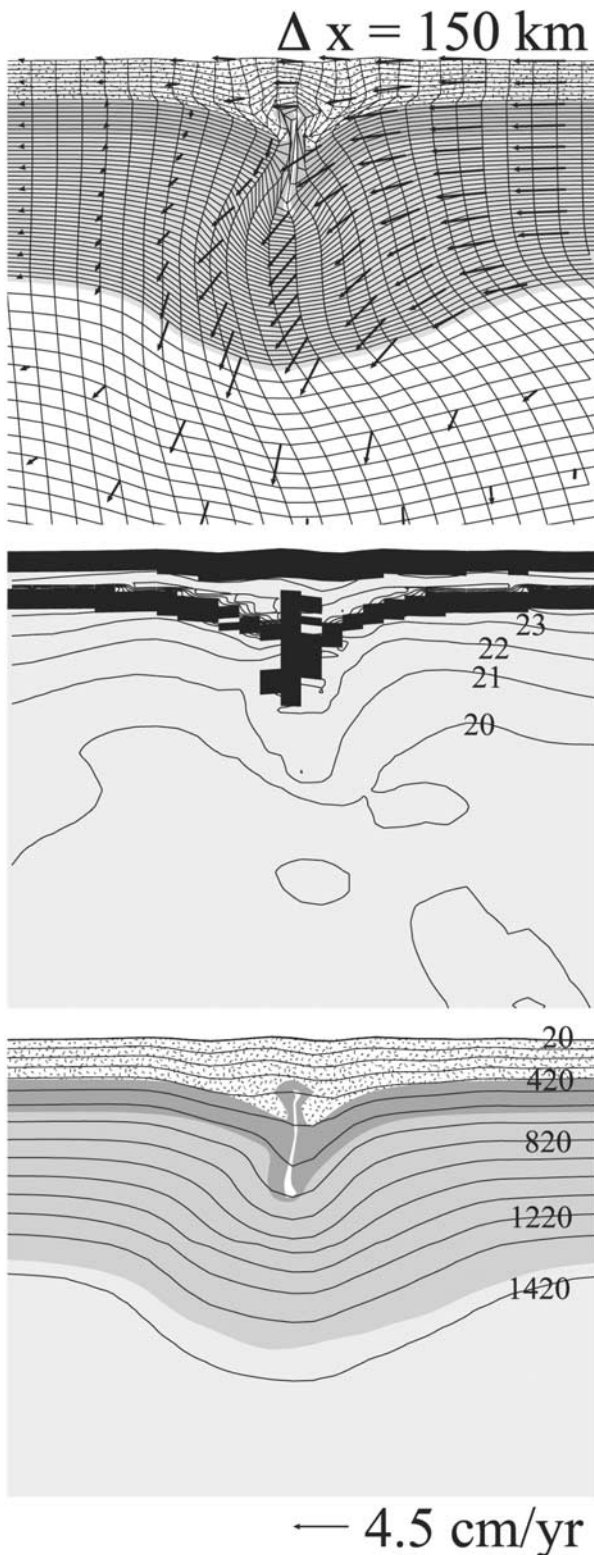


**Figure 12.** Evolution of EX10 at cumulative convergence  $\Delta x = 150$  km ( $\sim 3.3$  Myr). Same as reference model EX1, but triple imposed convergence rate to  $v_x = 4.5$  cm  $\text{yr}^{-1}$  (see Table 2). Top frame shows material regions, Lagrangian mesh and velocity vectors; middle frame plots plastic/viscous map and isotherms; bottom frame repeats material regions and plots log of effective viscosity (refer to Figure 3 for details).

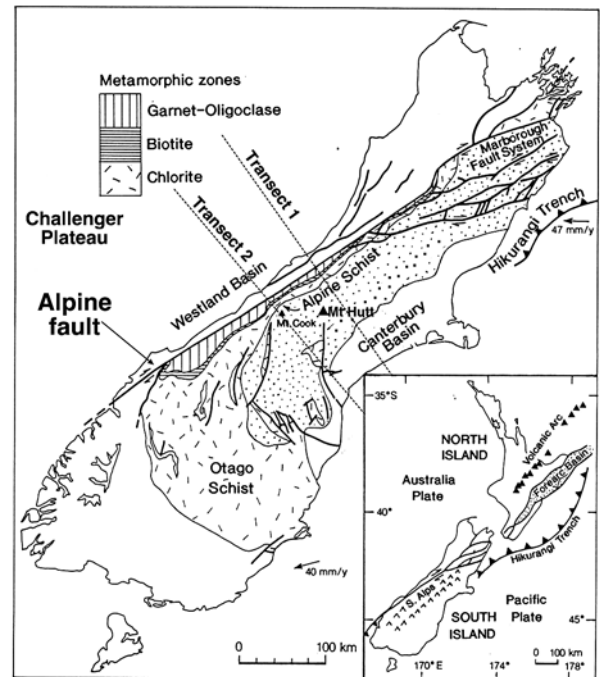


**Figure 13.** Map of South Island, New Zealand, showing relevant tectonic and geographic features. Inset illustrates the nature of the Australia-Pacific plate boundary in the region. Approximate location of the two SIGHT seismic transect lines from Stern *et al.* [2000] are marked. Adapted from Beaumont *et al.* [1996].

[Reyners and Cowan, 1993]. There is also evidence, however, that the upper continental crust is underlain by a high-velocity layer interpreted to be old oceanic crust [Reyners and Cowan, 1993]. To consider the influence of a basal oceanic crustal layer on the behavior of the models, a suite of numerical experiments was conducted in which a layer of  $\sim 8$ -km-thick material was included at the base of the crust (i.e., in place of a portion of region 2, Figure 2). The rheology of the layer was based on the nonlinear creep parameters for dry Maryland diabase from the laboratory experiments of Mackwell *et al.* [1998]. To model a wet diabase, the effective viscosity of this material was reduced by a factor of 10, corresponding approximately to the strength envelope of a Pikwitonei metamorphic granulite [Wilks and Carter, 1990; Mackwell *et al.*, 1998]. The numerical experiments, however, demonstrated that this model oceanic crust was similar in its behavior to the upper mantle lithosphere (uppermost region 2), and its presence made no appreciable difference to the evolution of the models. That is, the oceanic crust remained quite strongly attached to the underlying mantle lithosphere. Therefore, to simplify the model, this layer was omitted, and the oceanic crust may be conceptually considered as the uppermost  $\sim 8$  km of the olivine mantle lithosphere in the experiments EX1–EX10.

[40] To investigate deformation of the lithosphere in the context of South Island, New Zealand, we have shown most of the models advanced to an accumulated plate convergence of 150 km. Tectonic reconstructions suggest that over

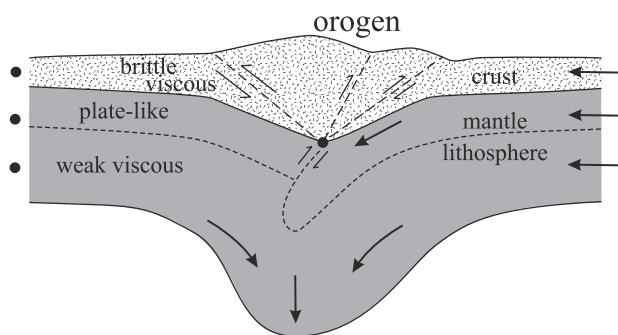


**Figure 14.** Conceptual model for deformation of the lithosphere across South Island, New Zealand. Brittle upper crust forms orogeny, and basal detachment zone partially decouples the crust from the mantle lithosphere. Uppermost mantle lithosphere is rigid and subducting in a plate-like manner. Lower mantle lithosphere is a weaker viscous region in which the root is developing as a gravitational instability. With this small amount of shortening, offset between center of orogeny and lithospheric root may be relatively small.

the last  $\sim 6.4$  Myr shortening across the island is 90 km across the center of the Alpine fault, with 70 km and 110 km at the southern and northern ends of the island, respectively [Walcott, 1998]. It is difficult to provide a precise calibration between observation and modeling, but this scale of shortening corresponds to an imposed convergence of  $\sim 100$ – $150$  km in the numerical experiments. This difficulty is partly caused by an initial convergence stage of 25–50 km before localization occurs in the models.

[41] While crustal deformation in the region has been quite well studied [e.g., Wellman, 1979; Koons, 1989; Norris *et al.*, 1990; Kamp and Tippett, 1993; Reyners and Cowan, 1993], it is only recently that observational constraints on the deep geodynamic evolution of the lithosphere beneath South Island, New Zealand, have become available. The main focus of our comparison of modeling results with observation concerns the nature of this lithospheric-scale deformation.

[42] Deep geophysical probing of the region has been carried out as part of the South Island Geophysical Transect (SIGHT) project [Davey *et al.*, 1998]. On the basis of predominantly seismic and gravity data from SIGHT Molnar *et al.* [1999] and Stern *et al.* [2000] argue that there is evidence that the mantle lithosphere is deforming by a style of distributed pure shear thickening (i.e., more akin to Figure 1a than Figure 1b). Stern *et al.* [2000] examine arrival delays of teleseismic  $P$  waves across the island (see Figure 13 for transect locations) and compare the observations with modeled travel time delays for various high-velocity subcrustal lithospheric structures. They determine that the best fit to the data is achieved with an approximately symmetric body of width 80–100 km, vertical height 100 km, and centered at a depth of 120 km. Their inference from these results is that the geometry of lithospheric thickening, in particular its apparent symmetry, precludes a subduction-style deformation of the mantle lithosphere (Figure 1b) and favors pure shear-type thickening.

[43] The numerical experiments that we have presented, however, suggest an alternative interpretation of the data.

Namely, the lithosphere may simultaneously exhibit both of these modes of behavior as the upper rigid portion of the mantle lithosphere underthrusts/subducts in a plate-like manner and the lower, weaker region thickens homogeneously (Figure 14). This type of behavior occurs in most models of the type described above when there is plastic strain softening. The olivine mantle lithosphere is effectively partitioned into a strong plate-like layer (consisting of both the plastic and high-viscosity regions) and an underlying lower-viscosity region which would participate in the gravitational instabilities. The rheological division of lithosphere into these two parts depends primarily on the composition of the mantle lithosphere, the ambient temperature, and the rate of convergence. The Hirth and Kohlstedt [1996] wet olivine mantle lithosphere (EX2), for example, has a significantly higher fraction of weak viscous mantle lithosphere ( $\sim 50\%$ ) than either the Chopra and Paterson [1984] wet Aheim ( $\sim 30\%$ , EX1) or the Hirth and Kohlstedt [1996] dry ( $\sim 25\%$ , EX3) models. The higher-temperature experiment (EX6) resulted in a weaker mantle lithosphere and therefore promoted a greater fraction of weak, unstable lithosphere.

[44] Our proposed model of combined upper plate underthrusting and viscous instability of the lower mantle lithosphere is also in general agreement with constraints from crustal modeling and observations for New Zealand. The asymmetry of geological structure and topography of the Southern Alps and position of the Alpine fault is consistent with deformation imposed by underthrusting/subduction of the Pacific plate mantle beneath the Australian plate [Beaumont *et al.*, 1996; Batt and Braun, 1999; Willett *et al.*, 2001]. The asymmetry of crustal deformation only allows inferences to be made concerning the dynamics of the uppermost part of the mantle lithosphere. Therefore these observations do not preclude contemporaneous viscous instability in the lower lithosphere.

[45] The modeling results also suggest that caution must be taken in using constraints from the general geometry of lithospheric thickening of the lithosphere (e.g., constraints like those used by Stern *et al.* [2000]) to draw strong conclusions regarding the dynamics of the region. During the early stages of collision any asymmetry in the model mantle lithosphere geometry caused by the underthrusting of one plate beneath another is not substantial. In EX1, for example, during the first 150 km of convergence the offset between the center of the lithospheric root and the maximum surface topography (i.e., orogen) is only  $\sim 10$  km (Figure 3b). While there is significant “subduction structure” within the mantle lithosphere (which is not necessarily seismically visible as a density contrast), the asymmetry in the overall structure of the lithosphere is quite subtle. Similarly, the other numerical experiments demonstrate relatively little overall asymmetry of lithospheric deformation.

[46] It should also be noted that the approximate dimensions of the lithospheric root for EX1 at  $\Delta x = 150$  km are compatible with those derived from the analyses of Stern *et al.* [2000] (as described above). The thickened mantle lithosphere in Figure 3b, for example, is  $\sim 100$  km wide and  $\sim 160$  km in vertical extent. A well-developed, rapidly downwelling viscous instability, as in the “hot lithosphere” model EX6, however, is not consistent with the geophysical



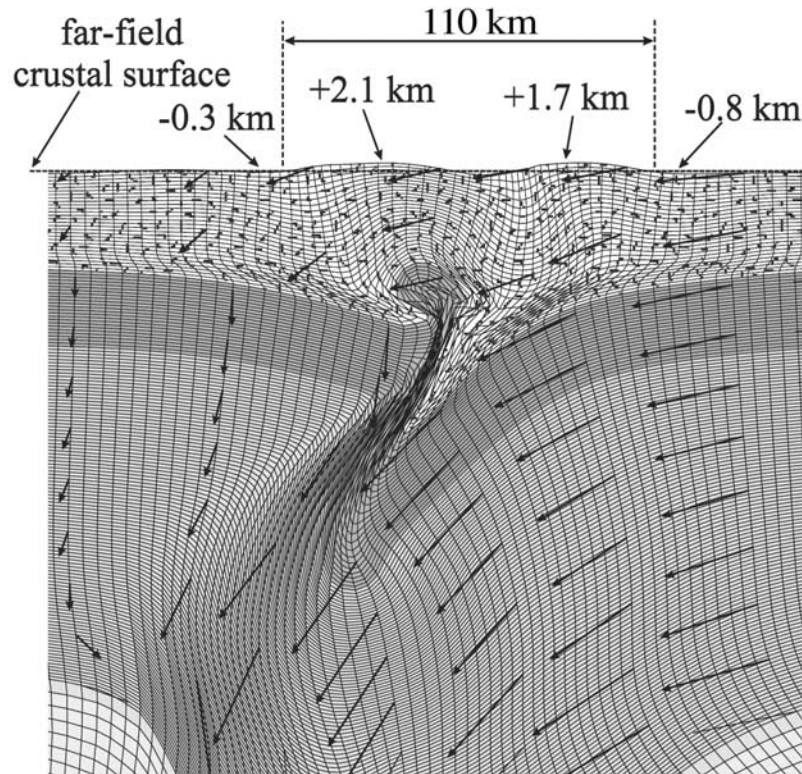


**Figure 15.** Zoom of lithospheric collision for EX1 at  $\Delta x = 150$  km. Various dimensions are highlighted including the elevation of the primary and secondary positive topography surface features, and major topographic depressions (all measured from the undisturbed far-field crustal surface).

observations. Direct comparisons are hindered as it is difficult to exactly reconcile imposed convergence in the model with observations from plate reconstructions. Furthermore, the dimensions given by *Stern et al.* [2000] are for a discrete velocity anomaly and are therefore somewhat incompatible with measurements of deformation of a continuous lithosphere.

[47] Although the study focuses on the evolution of the mantle lithosphere, the models also develop notable structure in the crust. Figure 15 magnifies the upper regions of the lithosphere for experiment EX1 after 150 km of convergence. Although not necessarily evident in Figure 3, it is clear that the free surface at the top of the solution space allows for significant topography to develop in response to the collision of the lithospheric plates. For example, there is a central uplift of amplitude  $\sim 2.1$  km (measured in reference to the top surface of undeformed, far-field crust) that has developed, along with a secondary peak of height  $\sim 1.7$  km. This orogen is  $\sim 110$  km in width and is bounded on each side by topographic lows. At a maximum the crustal thickness reaches  $\sim 38$  km and a hot, weak basal detachment extends 60–80 km in either direction from the center of the collision zone.

[48] To first order, these features are consistent with a general topographic profile across South Island (e.g., across the transect indicated on Figure 13). The primary positive topography in the model corresponds to the main belt of high topography on the western side of the island, the Southern Alps. The ranges reach elevations of the order

of 3000 m and are up to 100 km wide (i.e., perpendicular to strike). The secondary positive topography in the model may represent crustal deformation in response to detachment outside of the central mountain belt and may be analogous to uplifts such as the Mount Hutt range, an external basement uplift to the east of the primary alpine belt. The topographic lows which flank the central uplift region in the model are consistent with the location of sedimentary basins in New Zealand. A deep strike-parallel basin, the Westland Basin, occurs close to the western margin of the Southern Alps, and on the eastern side of the island the Canterbury Basin comprises a series of thin depositional sequences which formed through several local subsidence events. Despite the similarities noted here, an in-depth comparison with the upper crustal tectonics of South Island cannot be justified because the current models do not include the effects of surface denudation and deposition, processes known to have been important in the recent evolution of the continental collision zone in South Island.

[49] Although the model predicts the broad crustal features of South Island, New Zealand, structures corresponding to the Alpine fault (Figure 13) do not develop in the numerical experiments. Other geodynamical models, but at a crustal scale, have been successful in predicting the development of this large-scale shear zone [e.g., *Beaumont et al.*, 1996]. The difference is that the numerical models presented here both ignore surface processes and have significant thermal variations in material rheology. The latter leads to the development of a weak ductile region to



develop at the base of the crust which effectively decouples the crust from the mantle lithosphere at the collision zone (Figure 15). Thus horizontal stresses associated with the subducting mantle lithosphere are not as well transmitted to the overlying crust as in the *Beaumont et al.* [1996] models and apparently are not of sufficient magnitude to develop the a focused shear zone(s). Even *Beaumont et al.* [1996] required the model shear zone, equivalent to the Alpine fault, to be weak in order to achieve acceptable thrust uplift and exhumation. The effect of climate-coupled denudation focused on the western flank of the Southern Alps has also been shown to be potentially important in reinforcing thrust-sense development of the Alpine fault [*Beaumont et al.*, 1996]. This is reinforced by results from other crust-mantle collisional models not included here. Strongly denuded models, otherwise similar to that shown in Figure 15, develop retroshears resembling the Alpine fault through a strain localization feedback mechanism. The formation of the Alpine fault is also likely related to a preexisting zone of weakness associated with the component of strike-slip motion between the Pacific and Australian plates in the region. We disregard heterogeneities and preexisting structure in the crust for simplification in these models but admit that these may play a role in determining the style of crustal deformation during convergence [e.g., *Sutherland et al.*, 2000].

## 5. Discussion and Conclusions

[50] The numerical experiments suggest that during the initial stages of plate collision, the mantle lithosphere may be characterized by plate-like behavior associated with underthrusting/subduction of the upper regions and distributed thickening and Rayleigh-Taylor viscous instability of the lower portion (Figure 14). This combined style of deformation is consistent with the observed crustal structure in the collisional orogen of South Island, New Zealand, and seismic imaging of the geometry of the underlying lithosphere.

[51] In these experiments we have confined the models to consider relatively young and cool plate collisions, such as New Zealand. Over longer timescales of orogenic evolution it might be expected that there are significant variations in the dynamics of the system. For example, EX9 and especially EX10 show that the behavior of the mantle lithosphere during collision is sensitive to the plate convergence velocity. Therefore, through the lifetime of a collisional orogen, there may be several phases in which different behavioral modes of the mantle lithosphere dominate, as a consequence of changes in the large-scale plate motions. Modeling results demonstrate that an initial stage of convergence, followed by a dramatic decrease or cessation of convergence will cause a transition from initial subduction of the mantle lithosphere to viscous dripping and convective thinning of the lithosphere [*Pysklywec et al.*, 2000].

[52] One aspect of the models that defines their character and leads to asymmetric underthrusting is the development of localized deformation (i.e., shear zones) which cut the strong plastic model layers. Without the coupled plastic failure and ensuing strain softening, deformation is more diffuse. In the numerical experiments the decrease in the internal angle of friction,  $\phi$ , is chosen empirically. However,

there is evidence that persistent weak faults and shear zones significantly influence the architecture and pattern of strain partitioning in the crust [*Sibson*, 1977; *Handy*, 1989; *Holds-worth et al.*, 1997]. The possible mechanisms range from high transient or static fluid pressures, weakening by gouge [*Sibson*, 1990; *Streit*, 1997], or in polymineralic shears weak phyllosilicates may lead to significant weakening [*Bos and Spiers*, 2002]. Strain localization may also occur in the ductile regime [e.g., *Vissers et al.*, 1995; *Braun et al.*, 1999] which implies that underthrust/subduction styles of deformation may occur in mantle lithosphere even in the absence of the plastic instabilities that force focused shear in the viscous mantle lithosphere of the current models.

[53] The evolution of the lithosphere during later stage orogenesis will also likely be strongly influenced by the thermal state of the region. Even with the relatively cool, young orogens considered in the models, it was clear that the behavior of the lower crust and mantle lithosphere was very sensitive to temperature. In larger, more well-developed orogens such as the Himalayas, variations in the thermal regime would be much more pronounced and perhaps lead to alternate deformational styles from the numerical experiments. Furthermore, we omit in the models the influence of radioactive heat generation in the crust. This may become an important factor in controlling the nature of the crust-mantle interaction (e.g., the degree of detachment between these regions) and significantly alter the evolution of the crust, especially for case of thick crust lithosphere.

[54] A style of mantle lithosphere deformation that is often cited is “delamination” as defined by *Bird* [1979]. This process involves a peeling away of the complete mantle lithosphere layer, directly exposing the crust to upwelling asthenosphere. While other studies have shown evidence for this type of behavior [e.g., *Schott and Schmel-ing*, 1998], the numerical experiments did not show any such propensity for rollback of the whole mantle lithosphere. Instead, the underthrust slabs tended to weaken and detach from the upper lithosphere, rather than peel it back. Preliminary experiments indicate that delamination of the mantle lithosphere may occur within a particular geodynamic parameter space (e.g.,  $v$ ,  $T$ ) and with specific initial conditions (e.g., significant preexisting weak zones), which are not studied here.

[55] **Acknowledgments.** This work was funded by NSERC and Lithoprobe Supporting Geoscience grants to R.N.P. and C.B. C.B. also acknowledges support through the Inco Fellowship of the Canadian Institute for Advanced Research. We thank the Sean Willett and an anonymous reviewer for their constructive comments on the original manuscript. We also greatly appreciate Tim Stern providing a copy of the paper by *Stern et al.* [2000] prior to its publication. Lithoprobe contribution 1255.

## References

- Batt, G. E., and J. Braun, The tectonic evolution of the Southern Alps, New Zealand: Insights from fully thermally coupled dynamic modelling, *Geophys. J. Int.*, **136**(2), 403–420, 1999.
- Beaumont, C., P. J. J. Kamp, J. Hamilton, and P. Fullsack, The continental collision zone, South Island, New Zealand: Comparison of geodynamical models and observations, *J. Geophys. Res.*, **101**, 3333–3359, 1996.
- Beavan, J., et al., Crustal deformation during 1994–1998 due to oblique continental collision in the central Southern Alps, New Zealand, and implications for seismic potential of the Alpine Fault, *J. Geophys. Res.*, **104**, 25,233–25,255, 1999.

- Bird, P., Continental delamination and the Colorado Plateau, *J. Geophys. Res.*, **84**, 7561–7571, 1979.
- Bos, B., and C. J. Spiers, Frictional-viscous flow of phyllosilicate-bearing fault rock: Microphysical model and implications for crustal strength profiles, *J. Geophys. Res.*, **107**, 10.1029/2001JB000301, 2002.
- Braun, J., J. Chéry, A. Poliakov, D. Mainprice, A. Vauchez, A. Tomassi, and M. Daignieres, A simple parameterization of strain localization in the ductile regime due to grain size reduction: A case study for olivine, *J. Geophys. Res.*, **104**, 25,167–25,181, 1999.
- Buck, W. R., and M. N. Toksöz, Thermal effects of continental collisions: Thickening a variable viscosity lithosphere, *Tectonophysics*, **100**, 53–69, 1983.
- Chopra, P. N., and M. S. Paterson, The role of water in the deformation of dunite, *J. Geophys. Res.*, **89**, 7861–7876, 1984.
- Conrad, C. P., and P. Molnar, The growth of Rayleigh-Taylor-type instabilities in the lithosphere for various rheological and density structures, *Geophys. J. Int.*, **129**, 95–112, 1997.
- Davey, F. J., et al., Preliminary results from a geophysical study across a modern, continent-continent collisional plate boundary—The Southern Alps, *New Zealand, Tectonophysics*, **288**, 221–235, 1998.
- England, P., and G. A. Houseman, Extension during continental convergence, with application to the Tibetan Plateau, *J. Geophys. Res.*, **94**, 17,561–17,579, 1989.
- Fullsack, P., An arbitrary Lagrangian-Eulerian formulation for creeping flows and applications in tectonic models, *Geophys. J. Int.*, **120**, 1–23, 1995.
- Gleason, G. C., and J. Tullis, A flow law for dislocation creep of quartz aggregates determined with the molten salt cell, *Tectonophysics*, **247**, 1–23, 1995.
- Handy, M. R., Deformation regimes and the rheological evolution of fault zones in the lithosphere: The effects of pressure, temperature, grain size and time, *Tectonophysics*, **163**, 119–152, 1989.
- Hirth, G., and D. L. Kohlstedt, Water in the oceanic upper mantle: Implications for rheology, melt extraction and the evolution of the lithosphere, *Earth Planet. Sci. Lett.*, **144**, 93–108, 1996.
- Holdsworth, R. E., C. A. Butler, and A. M. Roberts, The recognition of reactivation during continental deformation, *J. Geol. Soc. London*, **154**, 73–78, 1997.
- Houseman, G. A., and P. Molnar, Gravitational (Rayleigh-Taylor) instability of a layer with non-linear viscosity and convective thinning of continental lithosphere, *Geophys. J. Int.*, **128**, 125–150, 1997.
- Houseman, G. A., D. P. McKenzie, and P. Molnar, Convective instability of a thickened boundary layer and its relevance for the thermal evolution of continental convergent belts, *J. Geophys. Res.*, **86**, 6115–6132, 1981.
- Houseman, G. A., E. A. Neil, and M. D. Kohler, Lithospheric instability beneath the Transverse Ranges of California, *J. Geophys. Res.*, **105**, 16,237–16,250, 2000.
- Jin, D., S.-I. Karato, and M. Obata, Mechanisms of shear localization in the continental lithosphere: Inference from the deformation microstructures of peridotites from the Ivrea zone, northwestern Italy, *J. Struct. Geol.*, **20**, 195–209, 1998.
- Kamp, P. J. J., and J. M. Tippet, Dynamics of Pacific plate crust in the South Island (New Zealand) zone of oblique continent-continent convergence, *J. Geophys. Res.*, **98**, 16,105–16,118, 1993.
- Koons, P. O., The topographic evolution of collisional mountain belts: A numerical look at the Southern Alps, *New Zealand, Am. J. Sci.*, **289**, 1041–1069, 1989.
- Lenardic, A., and W. M. Kaula, More thoughts on convergent crustal plateau formation and mantle dynamics with regard to Tibet, *J. Geophys. Res.*, **100**, 15,193–15,203, 1995.
- Landau, L. D., and E. M. Lifshitz, *Fluid Mechanics*, 536 pp., Pergamon, New York, 1959.
- Levander, A., E. D. Humphreys, G. Ekstrom, A. S. Meltzer, and P. M. Shearer, Proposed project would give unprecedented look under North America, *Eos Trans. AGU*, **80**(245), 250–251, 1999.
- Mackwell, S. J., M. E. Zimmerman, and D. L. Kohlstedt, High-temperature deformation of dry diabase with application to tectonics on Venus, *J. Geophys. Res.*, **103**, 975–984, 1998.
- Molnar, P., G. A. Houseman, and C. P. Conrad, Rayleigh-Taylor-type instability and convective thinning of mechanically thickened lithosphere: Effects of non-linear viscosity decreasing exponentially with depth and of horizontal shortening of the layer, *Geophys. J. Int.*, **133**, 568–584, 1998.
- Molnar, P., et al., Continuous deformation versus faulting through the continental lithosphere of New Zealand, *Science*, **286**, 516–519, 1999.
- Neil, E. A., and G. A. Houseman, Rayleigh-Taylor instability of the upper mantle and its role in intraplate orogeny, *Geophys. J. Int.*, **138**, 89–107, 1999.
- Norris, R. J., P. O. Koons, and A. F. Cooper, The obliquely-convergent plate boundary in the South Island of New Zealand: Implications for ancient collision zones, *J. Struct. Geol.*, **12**, 715–725, 1990.
- Poirier, J. P., Shear localization and shear instability in materials in the ductile field, *J. Struct. Geol.*, **2**, 135–142, 1980.
- Pysklywec, R. N., C. Beaumont, and P. Fullsack, Modeling the behavior of the continental mantle lithosphere during plate convergence, *Geology*, **28**, 655–658, 2000.
- Reyners, M., and H. Cowan, The transition from subduction to continental collision: Crustal structure in the north Canterbury region, *New Zealand, Geophys. J. Int.*, **115**, 1124–1136, 1993.
- Schott, B., and H. Schmeling, Delamination and detachment of a lithospheric root, *Tectonophysics*, **296**, 225–247, 1998.
- Sibson, R. H., Fault rocks and fault mechanisms, *J. Geol. Soc. London*, **13**, 191–213, 1977.
- Sibson, R. H., Conditions for fault-valve behaviour, in *Deformation Mechanisms, Rheology and Tectonics*, edited by R. J. Knipe and E. H. Rutter, *Geol. Soc. Spec. Publ.*, **54**, 15–28, 1990.
- Stern, T., P. Molnar, D. Okaya, and D. Eberhart-Philips, Teleseismic *P* wave delays and modes of shortening the mantle lithosphere beneath South Island New Zealand, *J. Geophys. Res.*, **105**, 21,615–21,631, 2000.
- Streit, J. E., Low frictional strength of upper crustal faults, *J. Geophys. Res.*, **102**, 24,619–24,626, 1997.
- Sutherland, R., F. Davey, and J. Beavan, Plate boundary deformation in South Island, New Zealand, is related to inherited lithospheric structure, *Earth Planet. Sci. Lett.*, **177**, 141–151, 2000.
- Tao, W. C., and R. J. O'Connell, Ablative subduction: A two-sided alternative to the conventional subduction model, *J. Geophys. Res.*, **97**, 8877–8904, 1992.
- Teng, L. S., C. T. Lee, Y. B. Tsai, and L.-Y. Hsiao, Slab breakoff as a mechanism for flipping of subduction polarity in Taiwan, *Geology*, **28**, 155–158, 2000.
- van Keken, P. E., S. D. King, H. Schmeling, U. R. Christensen, D. Neumeister, and M. P. Doin, A comparison of methods for the modeling of thermochemical convection, *J. Geophys. Res.*, **102**, 22,477–22,496, 1997.
- Vissers, R. L. M., M. R. Drury, E. H. Hoogerduijn Stratling, C. J. Spiers, and D. van der Wal, Mantle shear zones and their effects on lithosphere strength during continental breakup, *Tectonophysics*, **249**, 155–171, 1995.
- Walcott, R. I., Modes of oblique compression: Late Cenozoic tectonics of the South Island of New Zealand, *Rev. Geophys.*, **36**, 1–26, 1998.
- Wellman, H. W., An uplift map for the South Island of New Zealand, and a model for uplift of the Southern Alps, in *The Origin of the Southern Alps*, edited by R. I. Walcott and M. M. Cresswell, *Bull. R. Soc. N. Z.*, **18**, 13–20, 1979.
- Wilks, K. R., and N. L. Carter, Rheology of some continental lower crustal rocks, *Tectonophysics*, **182**, 57–77, 1990.
- Willett, S., C. Beaumont, and P. Fullsack, Mechanical model for the tectonics of doubly vergent compressional orogens, *Geology*, **21**, 371–374, 1993.
- Willett, S. D., R. Slingerland, and N. Hovius, Uplift, shortening, and steady state topography in active mountain belts, *Am. J. Sci.*, **301**, 455–485, 2001.
- Wilson, J. T., A new class of faults and their bearing on continental drift, *Nature*, **207**, 343–347, 1965.

C. Beaumont and P. Fullsack, Department of Oceanography, Dalhousie University, Halifax, Nova Scotia B3H 4J1, Canada. (chris.beaumont@dal.ca; philippe@adder.ocean.dal.ca)

R. N. Pysklywec, Department of Geology, University of Toronto, Toronto, Ontario, M5S 3B1 Canada. (russ@geology.utoronto.ca)